TU WIEN TECHNISCHE UNIVERSITÄT WIEN

Diplomarbeit

Determination of the intersection of metabolic volume and vascularization volume from hepatocellular carcinoma and its impact on life prolongation after Selective Internal Radiation Therapy

ausgeführt zum Zwecke der Erlangung des akademischen Grades eines

Diplom-Ingenieurs

unter der Leitung von

Ao.Univ.Prof. Dipl.-Ing. Dr.techn. Martin Gröschl
Institut für Angewandte Physik, TU Wien

Dipl.-Ing. Dr.techn. Albert Hirtl

Dr. Markus Hartenbach

Universitätsklinik für Radiologie und Nuklearmedizin

Medizinische Universität Wien

eingereicht an der Technischen Universität Wien

Fakultät für Physik

von

Stefan Weber

0725988

Gaismairsiedlung 15

39049 Sterzing Italien

Wien, Oktober 2015   _____

TECHNISCHE UNIVERSITÄT WIEN

Ich habe zur Kenntnis genommen, dass ich zur Drucklegung meiner Arbeit unter der Bezeichnung

Diplomarbeit

nur mit Bewilligung der Prüfungskommission berechtigt bin.

Ich erkläre weiters Eides statt, dass ich meine Diplomarbeit nach den anerkannten Grundsätzen für wissenschaftliche Abhandlungen selbstständig ausgeführt habe und alle verwendeten Hilfsmittel, insbesondere die zugrunde gelegte Literatur, genannt habe.

Weiters erkläre ich, dass ich dieses Diplomarbeitsthema bisher weder im In- noch Ausland (einer Beurteilerin/einem Beurteiler zur Begutachtung) in irgendeiner Form als Prüfungsarbeit vorgelegt habe und dass diese Arbeit mit der vom Begutachter beurteilten Arbeit übereinstimmt.

Wien, Oktober 2015   _____

Danksagung

Mein Dank gilt in erster Linie Herrn Ao.Univ.-Prof. Dr Martin Gröschl, der meine Arbeit betreut und begutachtet hat.

Daneben gilt mein Dank DI Dr. Albert Hirtl und Dr. Markus Hartenbach, die mir mit viel Geduld, Hilfsbereitschaft und Interesse zur Seite standen.

Nicht zuletzt möchte ich meiner Familie und meinen Freunden danken, welche mich während meines Studiums und der Anfertigung dieser Masterarbeit stets unterstützt und motiviert haben.

Kurzfassung

Das Hepatozelluläre Karzinom (HCC) ist eine bösartige Erkrankung der Hepatozyten (Leberzellen). Patienten mit intermediärem HCC Stadium (lokal fortgeschritten ohne Metastasen) erhalten palliative Lokalbehandlungen wie etwa die Transarterielle Chemoembolisation (TACE) oder die selektive interne Radiotherapie (SIRT). Hierbei werden den Patienten winzige, radioaktive Mikrosphären über die Leberarterie in den Tumor verabreicht. Diese bestrahlen einerseits den Tumor von innen und blockieren andererseits im Falle der Verwendung von SIR-Spheres® die Kapillargefäße des Tumors, sodass dieser „ausgehungert" und das Tumorwachstum erheblich verlangsamt wird. Eine prätherapeutisch-nuklearmedizinische Untersuchung, der sogenannte Leber-Lungen-Shunt-Scan mit Technetium (99mTc albumin aggregated (MAA)), stellt sicher, dass keine dieser radioaktiven Sphären über Verbindungen von der Leber zu anderen Organen gelangen kann. Hierbei werden, ähnlich wie bei der SIRT, mit Technetium beladene Mikrosphären über einen Katheter in die Leberarterie appliziert und mit einer Einzelphotonenemissiontomographie/Computer-Tomographie (Single Photon Emissionstomography – SPECT/CT) dargestellt. Diese Analyse erlaubt, dass man Rückschlüsse auf das arteriell-durchblutete Tumorvolumen ziehen kann.

Die Annahme, dass Patienten mit Tumoren, die gut vaskularisiert sind, besser von der SIRT profitieren, war Anlass und Idee dieser Arbeit. Eine volumetrische Analyse könnte hier in Zukunft ermöglichen, SIRT Kandidaten besser zu selektieren und deren Prognose präziser vorherzusagen.

In dieser Studie wurde einerseits die arterielle Versorgung, dargestellt mittels Technetium-MAA-Scan, und andereseits der Cholinstoffwechsel, dargestellt duch die eine Fluoroethylcholine- Positronen-Emissions-Tomographie (FEC-PET/CT), von 24 HCC Patienten miteinander kombiniert. Die Vereinigungsmenge dieser beiden Volumina ergibt das Tumorvolumen mit erhöhter arterieller Vaskularisierung. Die dadurch gewonnenen kombinierten Volumenparameter wurden anschließend mit den Überlebensdaten der Patienten (verbliebene Tage nach der Flourcholine-PET/CT bis zum Tod) sowie deren Tumormarkerwerten (Alphafoetoprotein - AFP) vor und nach der Behandlung verglichen.

Die Ergebnisse dieser Arbeit zeigen, dass Patienten mit geringeren metabolisch-aktiven Volumina in der Regel tendenziell eine höhere Lebenserwartung haben.

Grenzwertoptimierungskurven (Receiver Operating Characteristic – ROC) haben insgesamt gezeigt, dass Patienten mit einem metabolischen Volumen, das prozentuell eine hohe arterielle Blutversorgung aufweist, eine schlechtere Prognose haben als Patienten mit einem geringeren mikrovaskularisierten Tumor. Dies konnte auch mit einer multiplen logistischen Regressionsanalyse, bestehend aus mehreren unabhängigen Parametern, gezeigt werden. Jedoch sind aufgrund der geringen Patientenzahl die Einzelfaktoren in der multiplen logistischen Regressionsanalyse mit Ausnahme des hoch-vaskularisierten metabloischen Volumens nicht signifikant.

Die AFP-Werte in dieser Arbeit waren in den ROC-Analysen nicht signifikant. Dies kann wiederum damit erklärt werden, dass die Probandenzahl sehr niedrig ist.

Die vorliegende Arbeit zeigt das Potential dieser Methode, jedoch ist eine höhere Anzahl an Patienten notwendig, um eine quantitative Aussage treffen zu können.

Abstract

Hepatocellular carcinoma (HCC) is a severe disease of the hepatocytes (liver cells). Patients with intermediate HCC (locally advanced without metastasis) receive palliative local treatments, such as the trans-arterial chemoembolization (TACE) or the Selective Internal Radiation Therapy (SIRT). This therapy, utilizing small radioactive spheres, has shown promising results in prolonging the life expectancy of patients with unresectable HCC. These particles irradiate the tumor on the one hand, and block in the case of the usage of SIR-Spheres® the tumor capillaries on the other hand, yielding in "starvation" of the tumor and, therefore, a deceleration of its progression. An important requirement for patients considering this therapy is the assessment of the hepatopulmonary shunting. Shunts facilitate access from the liver to other organs, so that particles may dislocate, causing severe damages. The evaluation is performed by a technetium (99mTc) albumin aggregated (MAA) scan, where, similar to SIRT, small radiative spheres are injected into the hepatic artery. 99mTc emits 140 keV gamma rays which can be detected by Single Photon Emission Computed Tomography/Computed-Tomography (SPECT/CT). In addition, MAA-SPECT allows also a quantitative estimation of the tumor volume, which is highly vascularized and, therefore, well blood perfused.

The assumption that patients with tumors, which are highly vascularized, profit from SIRT, was the motivation of this thesis. A volumetric analysis should assist in the future the selection of possible candidates for SIRT and improve their prognosis.

The aim of this thesis was the volumetric analysis of 24 patients with HCC. The vascularization of the liver was determined by MAA-SPECT/CT. The metabolic volume was determined by a Fluoroethylcholine Positron-Emission-Tomography/Computed-Tomography (FEC-PET/CT). The combined volumes of vascularization and metabolism result in a volume which is highly metabolized and vascularized. These computations were analyzed and compared with the survival data (remaining days after FEC-PET/CT till death) and the tumor marker Alpha-fetoprotein (AFP) before and after the SIRT of each patient, respectively.

The results of this study suggest that patients with smaller tumor volumes have by trend an increased median survival. Receiver Operating Characteristic analyses (ROC) have shown that patients with a metabolic volume, which is highly vascularized,

have a poorer prognosis in comparison with patients with low-vascularized metabolic-active tumor volumes. A multiple logistic regression analysis, comprised of several parameters confirms these results. However, these individual factors except of the metabolic tumor volume are not significant presumably due to the small number of patients.

The ROC-analyses from the AFP-values were not significant in this study, again due to the low number of patients.

Investigations with more patients are required for a quantitative conclusion, yet, the present thesis shows the potential of this volumetric analysis regarding prognosis and life expectancy of HCC patients.

Contents

1   Introduction

Hepatocellular carcinoma (HCC) is the fifth most common malignancy and the third most common cause of cancer-related death worldwide [1-3]. Patients with intermediate-staged HCC are unsuitable for resection or liver transplantation (LT) and receive only palliative treatments, such as the trans-arterial chemoembolization (TACE) and the Selective Internal Radiation Therapy (SIRT). SIRT has shown promising results in prolonging patient's life expectancy using small radioactive spheres. These 20-30 µm large spheres, containing Yttrium-90 (90Y), are injected via the liver artery to the tumor region, where they irradiate the malignancy (with up to 200 Gy) and, in the case of SIR-Spheres®, block the tumor capillaries. SIRT uses the fact, that HCC is usually supplied by arterial blood vessels, while the normal liver tissue is supplied by the portal vein [4]. The blocking of the blood flow results ideally in starvation of the tumor, in a deceleration of its progression and, thus, in an increase of the life expectancy of the patient [5, 6].

A requirement for SIRT candidates is the assessment of the hepatopulmonary shunting. Shunts facilitate access from the liver to the other organs, such as the lung, causing severe damages. The evaluation is performed by a technetium (99mTc) albumin aggregated (MAA) scan, where, similar to SIRT, small particles are injected into the hepatic artery. 99mTc emits 140 keV gamma rays which can be detected by Single Photon Emission Computed Tomography (SPECT) [6].

With SIRT only regions with access to arterial blood vessels can be targeted. Hence, it is of paramount importance to locate the position of the malignancies precisely. The MAA-SPECT allows also a quantitative estimation of the vascularized tumor volume. However, it has a low resolution and there might be regions with higher vascularization without a malignancy or regions with homogeneous blood flow but with an isolated malignancy. Therefore, a second investigation method – a Fluoroethylcholine Positron-Emission-Tomography/Computed-Tomography (FEC-PET/CT) – is used in order to estimate the metabolic volume and thus the supposedly true location and size of the HCC. Finally, the intersection of the vascularization volume and the metabolic volume gives the metabolic-active tumor volume with high vascularization.

Knowing the vascularization of the HCC gives valuable information regarding applicability of SIRT and prognosis of HCC patients.

The basic aim of this study is to evaluate the prognostic parameters consisting of the vascularization volume, given by the MAA-SPECT, the metabolic tumor volume, given by the FEC-PET/CT, their intersection volume and the tumor marker Alpha-fetoprotein (AFP) in comparison to the overall survival of 24 HCC patients.

It is assumed that HCC patients with a high vascularization of their tumor should profit from SIRT resulting in an increased median survival. In contrast, patients with HCC that has a low vascularity or no arterial access should not be adequate for this therapy.

A volumetric analysis before SIRT application could optimize the selection of possible candidates and improve the precision of their prognosis.

2 Background

In this chapter an overview of the liver is given. The hepatocellular carcinoma and the palliative radioembolization treatment is explained subsequently. Furthermore, the medical imaging and diagnosis methods, which are used in this study, are described in more detail.
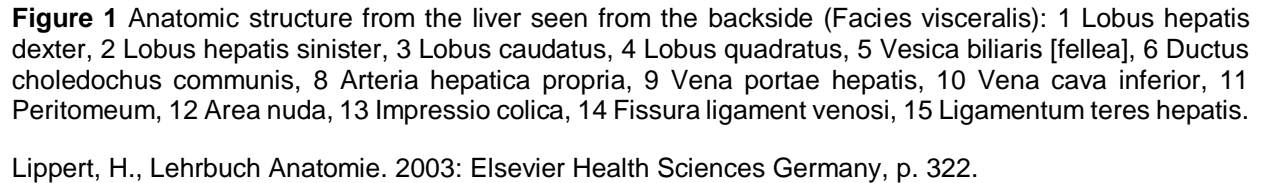
2.1 The Liver

The description of the liver is divided in a general part, where the structure and the main functions are mentioned, a subsequent blood supply part, a part describing the lobules and finally a list of the liver pathologies. The liver tumor is described in a separate chapter (see Chapter 2.2).

2.1.1 Structure and functions

The liver is a vital organ located in the upper right part of the abdomen, inferior to the diaphragm. The outer shape is basically formed by the neighboring organs and can be compared with a hemisphere. Further, it can be distinguished in two main areas: facies visceralis, lying shallowly on the stomach and the intestine, and the facies diaphragmatica, lying convexly on the diaphragmatic coupola.

The liver consists of four lobes; the Loubus hepatis dexter and sinister, which are separated by the main portal fissure, the Lobus quadratus in front of the Porta hepatis (portal vein), and the Lobus caudatus behind the Porta hepatis. *Figure 1* shows the anatomic structure of the liver. It is the biggest gland in the human body with a weight of about $1{,}5\,kg$ and has various important functions, such as:

- **Protein metabolism:** synthesis of plasma proteins and enzymes from amino acids, decomposition of proteins by synthesis of urea.
- **Carbohydrate metabolism:** synthesis, storage and decomposition of glycogen, synthesis of glucose from lactic acid and degradation products of proteins.
- **Lipid metabolism:** synthesis and decomposition of fatty acids, phospholipids, cholesterol, synthesis of about one liter bile per day containing bile acids, bile pigments, cholesterol, salts and mucus.
- **Inactivation and detoxification of hormones and impurities** by hydroxylation, oxidation, reduction, zygosis etc. [4].

Figure 1 Anatomic structure from the liver seen from the backside (Facies visceralis): 1 Lobus hepatis dexter, 2 Lobus hepatis sinister, 3 Lobus caudatus, 4 Lobus quadratus, 5 Vesica biliaris [fellea], 6 Ductus choledochus communis, 8 Arteria hepatica propria, 9 Vena portae hepatis, 10 Vena cava inferior, 11 Peritomeum, 12 Area nuda, 13 Impressio colica, 14 Fissura ligament venosi, 15 Ligamentum teres hepatis.

Lippert, H., Lehrbuch Anatomie. 2003: Elsevier Health Sciences Germany, p. 322.

2.1.2 Blood supply

The liver has a unique blood supply, due to the fact that it receives a dual blood supply from the vena portae hepatis (portal vein) and the arteria hepatica propria (see *Figure 2*). The liver is primarily supplied by the veins, which represent about ¾ of the liver blood volume. Secondly, the liver is supplied by the liver artery, which provides oxygen-rich blood. Although the artery supply accounts only for one quarter of the blood volume, it delivers one half of the oxygen to the liver tissue.

Blood vessels from the pancreas, stomach, gallbladder, spleen and intestines merge into the hepatic portal vein, delivering nutrient-rich blood from the gastVOIntestinal tract to the liver. Next to those vein vessels run the liver arteries, which branch into smaller vessels. This two afferent blood vessels run along with the intrahepatic bile ducts together in the so called trias hepatica or portal triad. The trias hepatica is embedded in connective tissue, accompanied by lymphatic vessels and forms
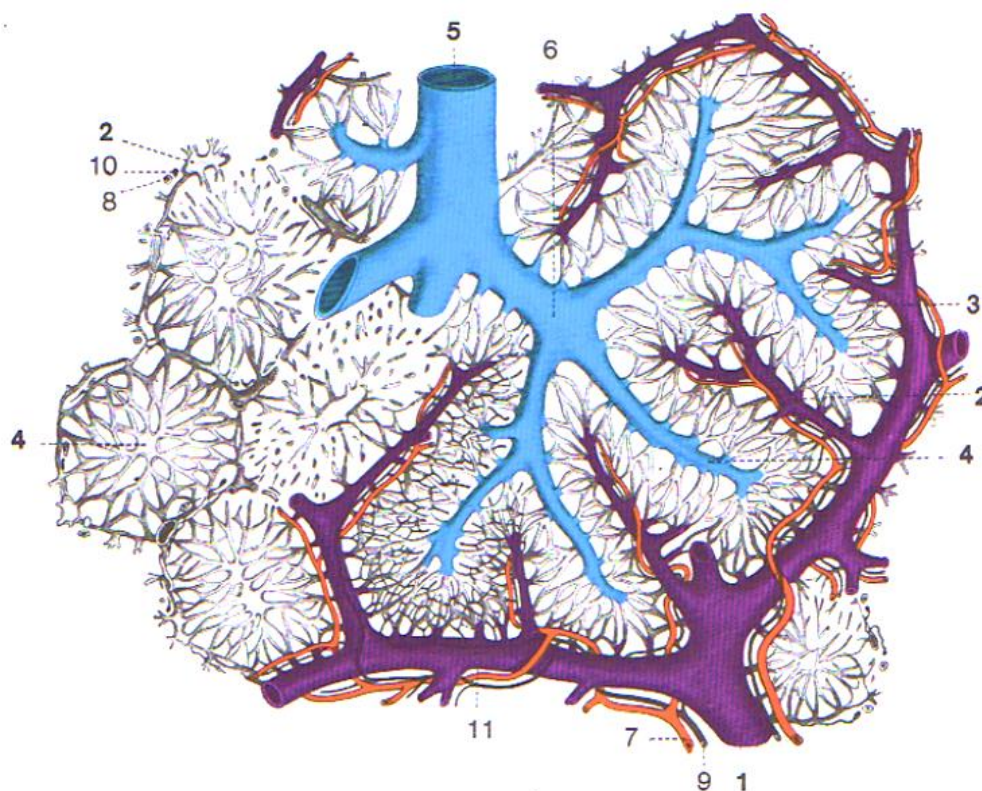
Figure 2 Blood vessels from the liver. 1 branch of the Vena portae hepatis, 2 Vena interlobularis, 3 Vasa capillaria sinusoidea, 4 Vena centralis, 5 branch of the Vena hepatica, 6 Vena sublobularis, 7 branch of the Arteria hepatica propria, 8 Arteria interlobularis, 9 Ducrulus bilifer, 10 Ductus bilifer interlobularis, 11 Canaliculus bilifer. Red: branches of the Arteria hepatica propria. Violet: branches of the Vena portae hepatis. Blue: branches of the Venae hepaticae.
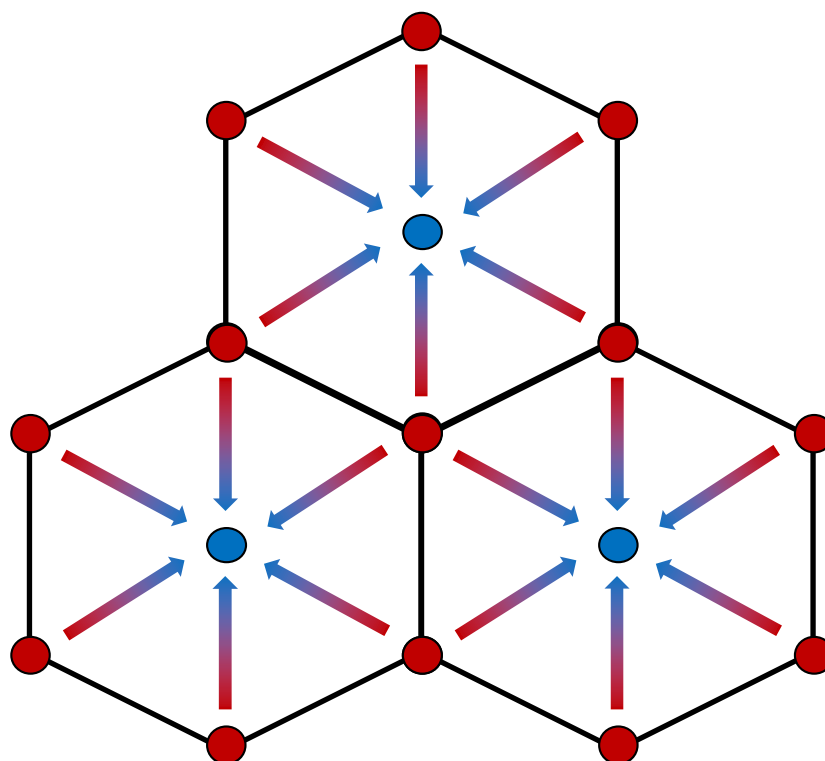
Lippert, H., Lehrbuch Anatomie. 2003: Elsevier Health Sciences Germany, p. 324.

triangular gores between the lobules. There, the blood is processed. The lobules and their functions are described in detail in the following Subchapter 2.1.3.

The central veins of the lobules merge into the sublobular veins of the liver, which flow into the Venae hepaticae and finally into the Vena cava inferior. The blood returns to the heart and is then delivered to the rest of the body.

2.1.3 Lobules

The liver lobules, or also known as arcini, are small hexagonal functional units in the liver. The internal structure of the liver consists of about 100,000 of these lobules. A single lobule has a central vein and is surrounded by six hepatic portal veins and six hepatic arteries (see *Figure 3*). Sinusoids (capillary-like tubes) connect these blood vessels so that the hepatic portal veins and the hepatic arteries meet the central vein. These sinusoids contain Kupffer cells, which are specialized macrophages

Figure 3 Idealized schemata of the lobules. The blue circles symbolize the Vena centralis. The red circles present the portal triad (trias hepatica).

Lippert, H., Lehrbuch Anatomie. 2003: Elsevier Health Sciences Germany, p. 328.

differentiated from monocytes, at their internal wall. Kupffer cells remove toxins from the portal veins. Further, they capture and break down old red blood cells.

Another important cell type is the hepatocyte. Hepatocytes are cubical epithelial cells with sides of $20 - 30\ \mu m$. They made up 80% of the liver's mass. They are responsible for the majority of the liver functions such as protein synthesis and storage, transformation of carbohydrates, synthesis of cholesterol, bile salt and phospholipids, detoxification and formation and secretion of bile.

2.1.4 Pathology

In the following section the most common liver diseases such as Hepatitis B and C, fatty liver disease and cirrhosis are briefly discussed. The main focus lies on hepatocellular carcinoma (HCC) and will therefore be described in a separate chapter in more detail.

Hepatitis B

Hepatitis B is a viral infection of the liver caused by the hepatitis B virus (HBV) and is mostly acute (90%) but can also be chronic. The virus is transmitted through contact

with body fluids of an infected person. About 240 million people worldwide have chronic infections and approximately 780.000 people die each year due to hepatitis B infection. Hepatitis B can be prevented by vaccine [7].

Hepatitis C

Hepatitis C is an infection of the liver induced by the hepatitis C virus (HCV). The hepatitis infection can both be acute and chronic. Acute HCV infection is considered only rarely life-threatening and is in most cases cured within 6 months. Chronic HCV infection represents a lifelong illness and bears the risk of developing cirrhosis. HCV is a blood borne virus and most commonly transmitted through poorly sterilized medical equipment, transfusions and intravenous drug use. Less common modes are by sexual transmission and giving birth from an infected mother. There is currently no vaccine available for HCV [8].

Fatty liver disease

Fatty liver disease (FLD) is a common disease of the liver where triglyceride fat is stored in large vacuoles in the liver cells. FLD is seen as a single, reversible disease and usually caused by obesity, dyslipidemia (lipid metabolism disruption), alcoholism, drugs, diabetes and hypertension [9].

Cirrhosis

Liver cirrhosis represents the final stage of an advanced chronic liver disease. Normally, development of cirrhosis takes several years to decades und is in its final stage irreversible. Treatment simply consists of preventing progression and complications. Liver transplantation is the only option for patients with advanced stage of cirrhosis. Cirrhosis is mainly caused by alcoholism, hepatitis B and hepatitis C, and FLD. Liver tissue is replaced by fibrosis and regenerative nodules resulting in the loss of the liver function, due to perfusion dysfunction. This leads to portal hypertension. Other common complications are ascites, hepatic encephalopathy and bleeding from dilated esophageal veins [9].

2.2   Hepatocellular Carcinoma

In this chapter some general information about HCC are given followed by etiology and risk factors, liver angiogenesis, HCC diagnosis, staging systems and the available treatments.

2.2.1 General information

Hepatocellular carcinoma is stated as the fifth most common form of malignancy and the third most common cause of cancer-related mortality worldwide [3, 10]. About 749.000 new cases are diagnosed every year [1]. HCC represents more than 90% of primary liver cancers beside others including intrahepatic cholangiocarcinoma, angiosarcoma, hepatoblastoma, mixed HCC and cholangiocarcinoma, and epithelioid hemangioendothelioma [11].

The incidence of new HCC cases is growing worldwide and is in Eastern Asia and Middle Africa about ten times higher compared to the Western world [12]. Generally, the incidence of HCC increases continuously with advancing age in all populations, reaching a peak at 70 years [13]. HCC is predominant in male with an estimated male to female ratio of 2.4 [1]. Incidence of HCC differs geographically (see *Figure 4*). The highest incidence rate of HCC is found in Eastern Asia sub-Saharan Africa and Melanesia, where about 85% of HCCs occur [1]. Developed regions show a low incidence with the exception of Southern Europe. There the incidence in men is notably higher compared to other developed regions [14].

2.2.2 Etiology and risk factors of HCC

In most cases, approximately 90%, HCC develops in the background of an underlying disease such as cirrhosis, a viral hepatitis B or C infection or aflatoxin exposure [1, 15]. The risk factors vary greatly in terms of geographical distribution (see *Table 1*). While in Africa and Eastern Asia, hepatitis B is the main risk factor, up to 60%, in the Western world it contributes only up to 20%. In return, chronic hepatitis C represents the major risk factor, up to $50 - 70\%$, in the Western world and only 20% in Africa and Eastern Asia. Alcohol is responsible for $10 - 20\%$ of HCC cases.

Overall, 54% of cases are associated with HBV infection, 31% with BCV infection and 15% with other causes. A very important risk factor for HCC is the cirrhotic liver, in which up to 80% of HCCs occur [16]. Cirrhosis as mentioned before is often caused
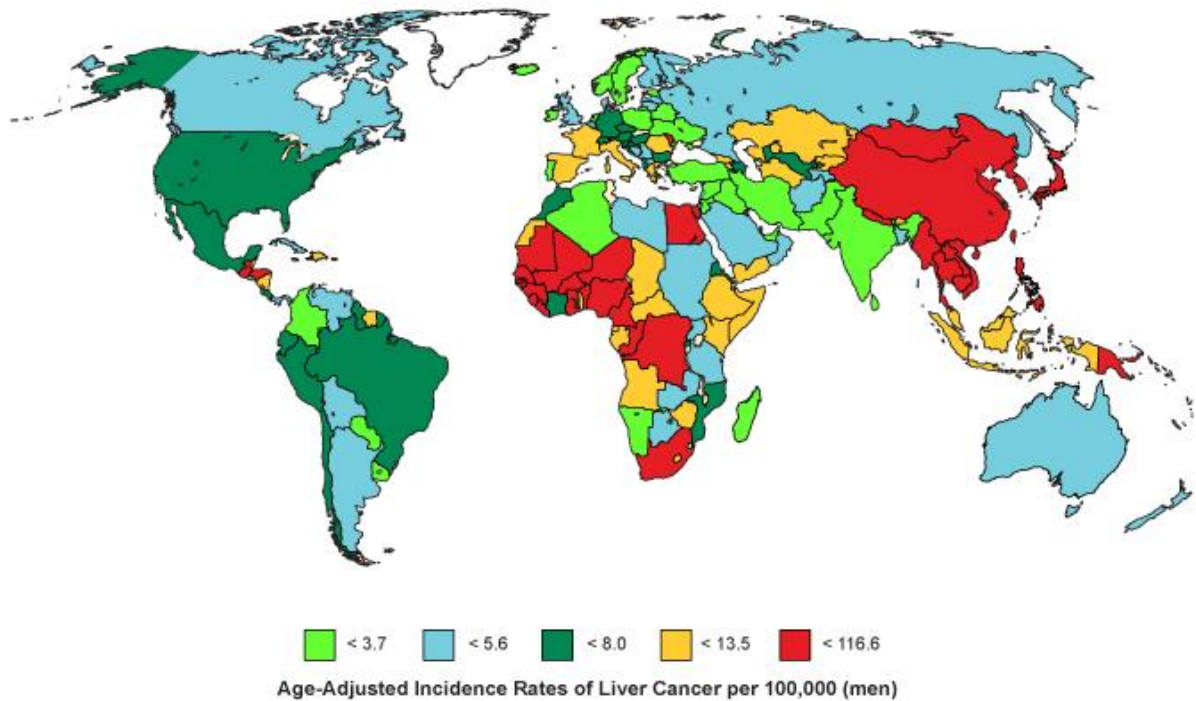
Figure 4 Geographical distribution of incidence rate of HCC worldwide.

International Agency for Research on Cancer 2013.

by chronic viral hepatitis, alcohol, non-alcoholic fatty liver disease and inherited metabolic diseases. One third of patients with cirrhosis will develop HCC in their lifetime [17]. Other additive co-factors for HCC development are obesity, diabetes, cigarette smoking, HIV infection and fatty liver disease [18-20].

Table 1 Geographical distribution of main risk factors for HCC worldwide.

Geographic area		AAIR	HCV	HBV	Alcohol	Others
		M/F	(%)	(%)	(%)	(%)
Europe		6.7/2.3	60-70	10-15	20	10
	Southern	10.5/3.3				
	Nothern	4.1/1.8				
North America		6.8/2.3	50-60	20	20	10 (NASH)
Asia and Africa			20	70	10	10 (Aflatoxin)
	Asia	21.6/8.2				
	China	23/9.6				
	Japan	20.5/7.8	70	10-20	10	10
Africa		1.6/5.3				
WORLD		16/6	31	54	15	

2.2.3 Tumor growth and angiogenesis

HCC develops in most cases from small dysplastic nodules, though neoplastic lesions to large HCC tumors [21]. HCC has three known growth patterns:

- Unifocal: defined as a single, massive tumor.
- Multifocal: Multiple malign tumor-nodules are spread across the whole liver.
- Diffuse infiltrative: The tumor growth is distributed diffusely across the whole liver [9].

All HCC forms tend heavily to invade surrounding blood vessels. During HCC development it secretes angiogenic growth factors while the expression of endogenous inhibitors are downregulated [21] resulting in a rapidly tumor growth and, consequently, to an increased need of oxygen and nutrient. Thus, HCC induces growth and generation of new blood vessels, termed angiogenesis and vasculogenesis, in order to gain access to the hepatic artery and to fulfill these demands. Those two mechanisms play a crucial role in HCC development [22]. However, these newly formed vessels are usually leaky and disorganized yielding in chaotic blood flow.

HCC is characterized by arterial hypervascularity in order to supply the tumor with oxygenated blood [23]. This fact is used by the radioembolization, explained in Chapter 2.3.

2.2.4 Diagnosis

Early tumor diagnosis is key for successful curative treatments. Today, early HCC diagnosis is achievable in $30 - 60\%$ of cases in developed regions [1]. This is thanks to new technologies and the implementation of surveillance policies[12]. Still, the detection of small nodules of about $2\ cm$ represents a diagnostic challenge due to the fact that they are difficult to characterize by pathological and radiological examination [24, 25].

In terms of cost-effectiveness there is an urgent need to discriminate nodules as preneoplastic lesions from early HCC. One-third of dysplastic lesions develops a malignant phenotype and should be monitored with regular imaging studies [26]. However, early HCCs are treated with curative procedures including resection, transplantation and percutaneous ablation [1, 27]. Biopsy was until 2000 the conventional diagnosis mode for HCC, but had several limitations:

- it proved problematic to reach certain locations

- the recognition of stromal invasion, which represents the most relevant criteria, is very difficult and therefore an accurate differentiation between high-grade dysplastic nodules and early HCC [28]

- it bears the risk of complications; for instance needle-track seeding and bleeding [29].

Nowadays non-invasive radiological diagnosis of early HCC is based on the combination of laboratory findings and imaging. The latter is achieved by the determination of the contrast up-take in the arterial phase with MRI, CT, US or angiography. However, biopsy or tissue biomarkers as well as Alpha-1-Fetoprotein (AFP) levels are still required in most instances. AFP is a glycoprotein found in the human fetus. After birth, the AFP level decrease rapidly. The function of AFP in adult humans is not yet clearly understood. In oncology, AFP is the most widely used biomarker to detect tumors in non-pregnant women, men, and children.

In order to define the stage and the treatment strategy of a tumor, the determination of the tumor extension is crucial. 4-phase multidetector CT and dynamic contrast-enhanced MRI have proven to be very effective imagine techniques in order to detect tumors smaller than $2\ cm$. Contrast-enhanced ultrasound and PET-based imaging are not accurate enough to stage early tumors [1].

2.2.5 Staging systems

The goal of classifying cancer is to provide prognosis and the adequate treatment for a suitable candidate. The fundamental clinical prognostic factors for patients with HCC are tumor status, liver function and the general health status. The tumor status is defined by the size and number of nodules. In addition, it includes information about extrahepatic spread and the presence of vascular invasion. The liver function is defined by the Child-Pugh's class and contains information of albumin, bilirubin, ascites and portal hypertension. Finally, the general health status is described by the ECOG classification and the existence of symptoms [1, 30].

In comparison to most solid tumors, patients with HCC suffer from two life-threatening diseases such as cancer and cirrhosis. This fact complicates the prognostic determination [31]. There exist several staging systems for HCC. In the section below

the most commonly used classification, which is the Barcelona-Clínic Liver Cancer (BCLC) classification, is described.

The Barcelona-Clínic Liver Cancer (BCLC) classification is nowadays commonly used as the standard classification for HCC and is currently recommended by the European Association for the Study of the Liver (EASL) and the American Association for the Study of Liver Diseases (AASLD) [1, 32]. This classification provides a correlation between the tumor status, liver function, health performance status, underlying disease, treatment strategy and prognosis [33]. It is constantly evolving by novel advancements in order to improve prognosis and management of HCC [1]. An advantage of the BCLC classification is that it divides patients with early HCC, who would benefit from curative treatments, from those with advanced tumor stages, who would benefit rather from palliative therapies [10].

The BCLC classification divides patients with HCC in five stages 0, A, B, C and D. These stages include information about the tumor status, liver performance, health status and median survival. For each tumor stage the standard of care and the appropriate treatment strategy is defined (see *Figure 5*). The single treatments either curative or palliative are describes in more detail in the next chapter.

- BCLC stage 0 represents the *very early HCC*, where a single tumor smaller than $2\,cm$ in diameter and without any vascular invasion is present. Furthermore, the patient shows well-preserved liver function and a good health status (Child-Pugh A class and ECOG 0 respectively). The diagnosis rate of patients with in this stage in the Western world is around $5-10\%$, while in Japan the value is almost 30%, due to implementations of surveillance programs [34]. Curative treatments such as resection or liver transplantation guarantee an $80-90\%$ survival rate within 5 year of patient at this stage, local ablation around 70% [35, 36].

- BCLC stage A or *early HCC* includes patients with single tumors larger than 2 cm or 3 nodules smaller than $3\,cm$ of diameter. Patients at this stage present a good health status (ECOG 0) and good liver functions (Child-Pugh A or B). Resection, transplantation, percutaneous ethanol injection (PEI) and radiofrequency ablation (RFA) are the recommended curative treatments at this stage. The median survival is estimated to be around 36 months, which
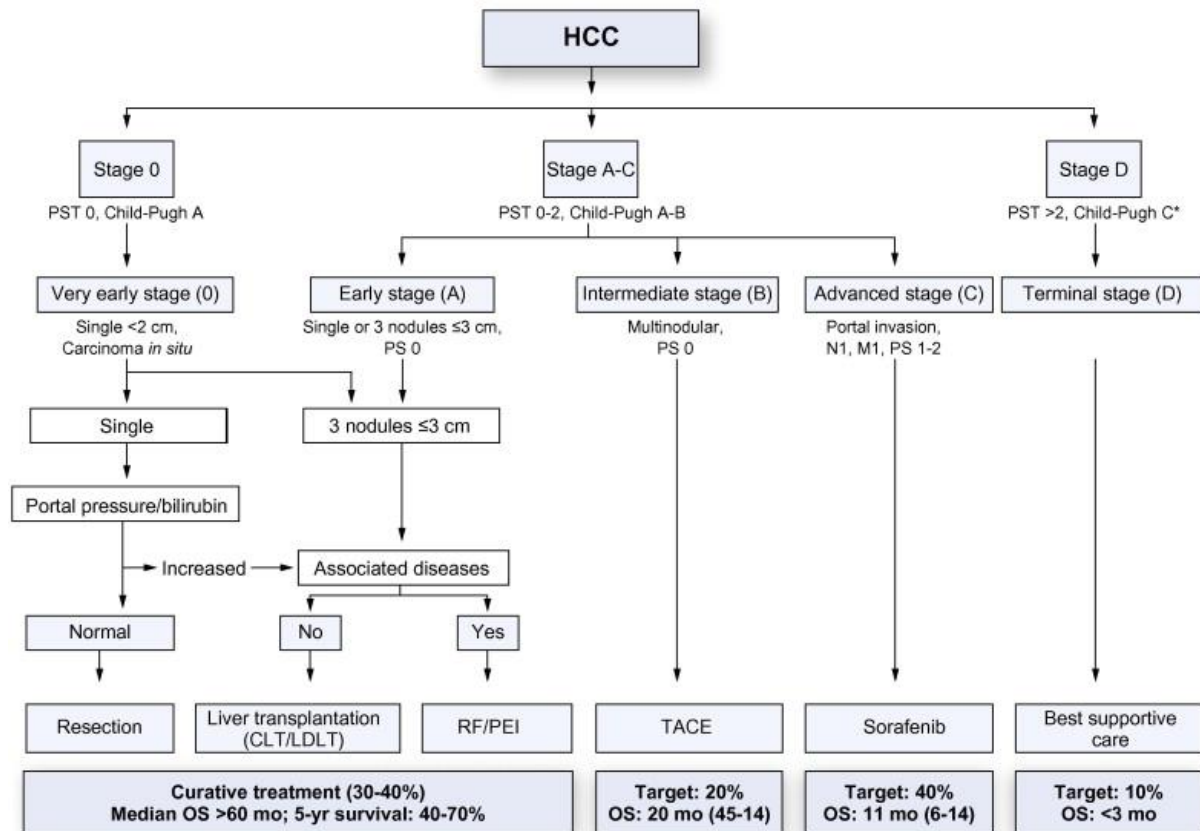
Figure 5 BCLC staging system and treatment strategy, 2011.

European Association for the Study of the Liver and European Organisation for Research Treatment of Cancer, EASL-EORTC clinical practice guidelines: management of hepatocellular carcinoma. J Hepatol, 2012. 56(4): p. 920.

correlates to $50 - 70\%$ at 5 year after resection, liver transplantation or local ablation [1, 12].

- BCLC stage B describes the *intermediate HCC.* HCC patients with tumors at this stage are considered unresectable. They present a poor health status and can be treated only palliative with chemoembolization (TACE) or rarely radioembolization (SIRT). The predicted median survival of untreated HCC patients at this stage is around 16 months [37] or rather 49% at 2 years [38]. The above mentioned palliative methods can extend the median survival up to $19 - 20$ months [37].

- BCLC stage C represents the *advanced HCC.* Patients at this stage bear a dismal prognosis due to cancer related-symptoms, poor health status, macrovascular invasion and extrahepatic spread. The median survival is expected to be 6 months [30] or 25% at 1 year [38], but varies according to the

status of the liver function. Patients with well-preserved liver function can reach a median survival of 7 months. In contrast, patients with severe liver impairments have a median life expectancy of only 5 months [39]. The standard-of-care for patients at the advanced HCC stage is the treatment with Sorafenib [39].

- BCLC stage D *or end-stage HCC* is characterized by tumors which lead to very poor performance status and liver functions, resulting in a severe tumor-related disability [1]. Patients with end-stage disease have a median survival of $3-4$ months [33] or 11% at 1 year [38]. The goal at this stage is to provide the best supportive care for the patients.

In this study, patients with intermediate HCC are investigated. According to the objectives stated above, only patients without any metastasis were chosen.

2.2.6 Treatments

In this section, the above-mentioned curative and palliative treatments are briefly described. The focus in this study lies on the radioembolization therapy, which will be discussed in Chapter 2.3 in more detail.

Resection

Surgical resection is the first-line treatment option for a small number of patients with early-staged disease, well-preserved liver functions and no underlying cirrhosis. Candidates which fulfill these criteria have a nearly 70% five-year survival. However, surgical resection bears a high risk of recurrence. There has been reported a five-year recurrence rate of 70% after liver resection of early-staged HCC. Recurrence within two years after resection is caused mainly by local invasion or intrahepatic metastasis. In contrast, recurrence emerging after two years is mainly related to *de novo* tumor formation. Resection on patients with cirrhosis has an increased risk of hepatic decompensation [40]. Portal hypertension represents a relative contraindication for surgical resection in cirrhotic patients.Studies have shown that a hepatic venous pressure gradient larger than 10 mmHg leads to a poor long-term outcome [32, 41]. In summary, surgical resection is only recommended for patients with small single tumor nodules and well-preserved liver function [1, 10, 27].

Liver transplantation

Liver transplantation (LT) represents a potentially curative treatment recommended for patients with single tumors smaller than 5 cm or up to 3 lesions not larger than 3 cm each (Milan Criteria), decompensated cirrhosis and advanced liver dysfunction [10]. The 5-year survival rate for appropriate candidates is 75% and the recurrence rate is less than 15% [42]. In theory, LT would simultaneously cure the tumor and the underlying cirrhosis. A major drawback of LT is the long waiting time for transplantation due to the scarcity of donors [1, 27].

Local ablation

Local ablation is recommended for patients at early stages who are not suitable for surgical resection and LT. Tumor ablation can be performed by using chemical or physical methods. Chemical ablation for tumor destruction includes the usage of absolute alcohols or acetic acids, such as the percutaneous ethanol injection (PEI). PEI induces coagulative necrosis caused by cellular dehydration, chemical occlusion of small tumor vessels and protein denaturation. Patients with nodules smaller than 5 cm in diameter undergoing PEI have a five-year survival rate of 47-53%. The high local recurrence rate of up to 43% presents the major limitation for PEI [43].

Physical ablation can be achieved by heating the tumor tissue up to 100°C, including radiofrequency ablation (RFA), microwave ablation (MWA) and laser ablation. Another physical ablation technique is the so called cryoablation, which freezes the tissue at -20°C and -60°C.

Currently, RFA is the most commonly applied treatment for patients not suitable for surgical therapies. The reason for this is that the energy derived from the RFA induces coagulative necrosis of the tumor, yielding in the formation of a safety ring in the peritumoral tissue and the elimination of small undetected satellites. Thus, RFA is associated with a very low local recurrence rate of less than 1% and has a five-year survival rate of 40%-70% for lesions smaller than 2 cm. For patients with tumors of 2-5 cm in diameter RFA has still the better anticancer effect than PEI [27, 36].

Chemoembolization

Chemoembolization is recommended for patients with unresectable HCC at intermediate stage as a palliative therapy option. HCC at this stage, i.e. a large single

nodule smaller than 5 cm in diameter and compensated liver function[10], has in most cases already an arterial access and receives therefore 90% of its blood by the hepatic artery [27]. The trans-arterial chemoembolization (TACE) utilizes this fact by blocking the blood supply with small particles of about 100-500 μm and by inducing tumor necrosis with cytotoxic agents. This results in a strong cytotoxic and ischemic effect which delays the tumor progression significantly. The median survival for patients rises from about 16 months to 20 months if treated with TACE.

Chemotherapy

HCC is one of the most chemo-resistant tumor types. The existence of two diseases complicates the application of a chemotherapy because cirrhosis can enhance the toxicity of the chemotherapeutic drugs by perturbing their metabolism. Until 2007 no systemic chemotherapy was recommended for patients with advanced HCC. Sorafenib arose as one of the first effective treatments after long years of research and is currently the standard-of-car for patients with advanced-stage HCC [1]. Sorafenib is a drug with antiproliferative and antiangiogenic effects [44]. More precisely, it is a multi-tyrosine kinase inhibitor administered orally, which prevents the uncontrolled growth of the hepatocytes and, thus, the tumor progression [10].

In a trial, sorafenib has shown positive survival results by increasing the median survival from 7.9 months in the placebo group to 10.7 months in the sorafenib group [39]. The combination with other systemic chemotherapeutic agents, has shown some survival advantage compared to sorafenib alone [10].

2.3 Radioembolization

Radioembolization or Selective Internal radiation therapy (SIRT) is a radiation therapy to treat unresectable HCC and liver metastasis. In this therapy, tiny glass or resin microspheres containing Yttrium-90 (90Y) are injected into the liver artery. Given the hypervascularity of HCC, these microspheres will be preferentially delivered to the tumor-bearing area and get stuck at the narrow-branched pathologic tumor vessels. During this process, the radioactive material (up to 200 Gy) destroys the tumor from inside and spares healthy tissue due to its short irradiation range. Further, by blocking the blood flow with the microspheres the tumor is starved out [45, 46]. In contrast to TACE, SIRT uses much smaller particles of about 35 µm, which do not cause ischemia in the tumor tissue [10].

An important requirement for patients considering SIRT is the assessment of hepatopulmonary shunting. Shunts facilitate access from the liver to the lung. Radioactive microspheres traveling along those paths during therapy can cause severe complications, like the adverse side effect of radiation pneumonitis. The evaluation is performed by a technetium (99mTc) albumin aggregated (MAA) scan.

Similar to the SIRT microspheres, small particles are labeled with a radioactive material and injected into the hepatic artery. 99mTc emits detectable 140 keV gamma rays which can be detected in the body by SPECT, measuring the percentage of particles that shunts to the lung. Assuming the majority of the radioactive particles remains in the liver, a decreased likelihood of them traveling to the lung can be expected and, furthermore, for this study a quantitative volume estimation of areas with increased vascularization can be determined (see Chapter 3.4.2). Patients with a high shunting percentage are unsuitable for this therapy.

In comparison to TACE, SIRT was associated with fewer side effects and a better response rate, but a similar median survival of about 20 months [47]. This therapy technique appears very promising. However, the costs associated with SIRT may limit a wide use [10].

2.4   Single Photon Emission Computed Tomography

In this section the Single Photon Emission Computed Tomography (SPECT) is described. First of all the general concepts of radionuclide imaging are explained. Then the gamma camera with its components is introduced. Afterwards its detection concept is elucidated. Finally the step from the gamma camera to SPECT is explained. The following paragraphs are based on the book from Cherry et al. 2012 Physics in Nuclear Medicine, chapter 13 and chapter 17 [48, 49].

2.4.1 General concepts of radionuclide imaging in SPECT

The main goal of radionuclide imaging is to gain an image of the distribution of a radioactively labeled material, which was administered into a patient before examination. The emission from the radioactivity is then detected and recorded with external radiation detectors located outside the patients. In order to detect such emissions on external radiation detectors, the rays need sufficient energy to penetrate the body tissue, especially for radioactively labeled substances in deep-lying organs. Gamma (γ) rays with energies about 80 to 500 keV are ideal for that purpose, while alpha and beta rays can penetrate the body tissue only a few millimeters and cannot escape the body.

Furthermore, γ-rays at such low energies can be shielded with little amount of lead and can be captured easily with dense scintillators. Commonly used scintillators are Sodium iodide [NaI(Tl)] scintillators. They provide good detection efficiency for γ-rays and are capable of energy discrimination. This becomes important when γ-rays undergo Compton scattering which alter their energies and directions. Those γ-rays have lost their positional information and can be discarded regarding their reduced energies.

2.4.2 System components

For the formation of an image with the gamma camera, a few essential components are required, such as a collimator, a [NaI(Tl)] scintillation crystal, a light guide and finally an array of photomultiplier (PM) tubes (see *Figure 6*). The collimator, mostly a lead plate of a few millimeter thickness with small cylindrical holes, guarantees that only rays parallel to those holes reach the scintillation crystal, providing a projected image of the γ-ray distribution. The remaining oblique photons are absorbed in the
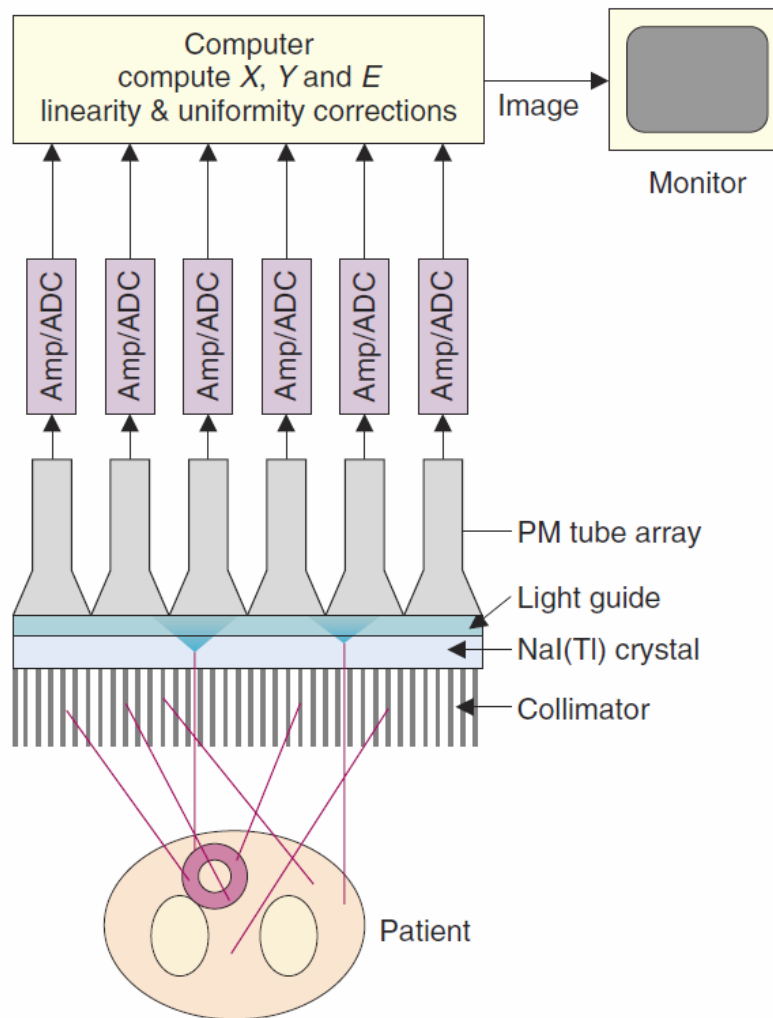
Figure 6 Principal and main components of a gamma camera.

Cherry et al., 2012 in Physics in Nuclear Medicine p.196.

collimator. The core component represents the large scintillation crystal, where the incoming γ-rays are converted to light. To the back of the scintillation crystal, an array of PM is coupled optically. Afterwards, the signal from each PM tube is amplified and digitized by an analog-to-digital converter. In comparison to one single PM, an array of PM is capable of determine the X-Y location of each scintillation event by weighting the PM tube signals. Another important feature, discussed before, is the capability of energy discrimination. Each individual event is analyzed for its energy by summing up the signals from all PM tubes. If the pulse amplitude of an event corresponds with the selected energy window it is accepted and its X-Y coordinate determined.

The gamma camera is mostly used for static imaging studies. Here, an image from an unchanging radionuclide distribution over an extended imaging time is created. Whole-body-scans can be achieved by scanning the entire patient and adding up the single contiguous images. This can be realized by moving either the gamma camera or the

bed with the patient. Dynamic imaging studies are used when changes in the radionuclide distribution are of interest, for instance the uptake rate or clearance for a tracer in an organ of interest. Further, by synchronizing the camera to an electrocardiogram signal, images of the heart in different phases of the cardiac cycle, can be obtained, providing relevant information on cardiac function.

NaI(Tl) detector crystal: The gamma camera consist of a single large NaI(Tl) detector crystal, usually 60 x 40 centimeter. This compound with a density of $\rho=3.67$ g/cm3 represents a very efficient absorber for γ-rays in the range of 50-250 keV, because here the photoelectric absorption is predominant. For energies above 250 keV Compton scattering is predominant and therefore larger volumes of NaI(Tl) crystal are required for efficient detection. The thickness generally ranges from 6- to 12.5 millimeter and is a tradeoff between detection efficiency and intrinsic resolution.

The NaI(Tl) crystal is surrounded by TiO_2, which represents a highly reflective material to minimize the light losses. The production of detection crystals consisting of NaI(Tl) is inexpensive and the light yield sufficient high. However, this material is very fragile and easily fractured by temperature changes and humidity. Therefore, an aluminum case outside the TiO_2 and the detector crystal seals and protects them from moisture. An optical glass, mounted on the back surface of the detector crystal, allows the scintillation light to reach the PM tubes (see *Figure 7*).

The PM are arranged in a hexagonal pattern to maximize the covered area. Usually, they are cylindrical and have a diameter of about 5 cm. Modern gamma cameras have
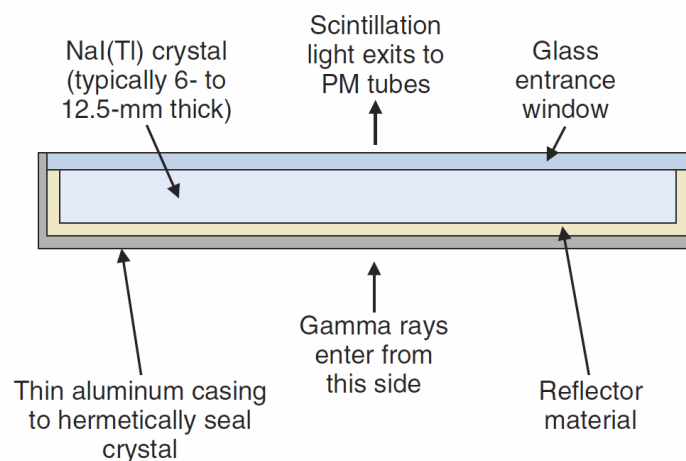
Figure 7 Cross section of a NaI(Tl) detector crystal. Cherry et al., 2012 in Physics in Nuclear Medicine p.197.

about 30 to 100 PM to cover the entire crystal area. Each PM is encased in a thin magnetic shield in order to cancel the influence of the magnetic field of the earth.

The light guide is positioned between the detector crystal and the PM tubes. Its function is to increase the light collection efficiency by guiding the scintillation light into the PM tubes and away from the gaps in between. The detector crystal is enclosed together with the PM tube array in a light-tight protective housing.

Collimators: In order to acquire an image with the gamma camera, it is necessary to project the γ-rays from the original source distribution onto the detector. Since γ-rays cannot be focused using lenses like for visible light, the principle of absorptive collimation must be applied. This means, by using an absorptive collimation, only γ-rays of a certain direction are allowed to reach the detector. Those, which do not travel in the proper direction are absorbed in the collimator. Therefore, a lead collimator with an approximate thickness of a few millimeters and small holes is mounted in front of the crystal (see *Figure 6*). The drawback of this method is, that most of potentially useful radiation is stopped by the absorptive collimator, leading to fewer counts at the detector and so to a relatively poor image quality. There exists four different types of collimators: parallel-hole-, pinhole-, diverging- and converging collimator (see Figure 8).

The pinhole collimator (see Figure 8 *A*) contains a small pinhole aperture in a piece of heavy metal, such as lead, tungsten or platinum. The aperture is typically located 20 to 25 centimeter away from the detector within a lead cone. Gamma rays from the source distribution travelling through the pinhole aperture project an inverted and magnified image on the detector. This method is most commonly used for imaging of small organs, such as the thyroid.

The parallel-hole collimator (see *Figure 8 B*) is the most commonly used collimator in nuclear medicine. The holes are shaped parallel from led foils. The walls between the holes are called septa. These septa absorb all γ-rays, which have not the proper travel direction and prevent them from traveling from one hole to the next. With a parallel-hole-collimator, the image is of the same size as the source distribution.

The diverging collimator (see *Figure 8 C*) consist of holes, which diverge from the detector face, typically 40-50 centimeter behind the collimator. The result is a
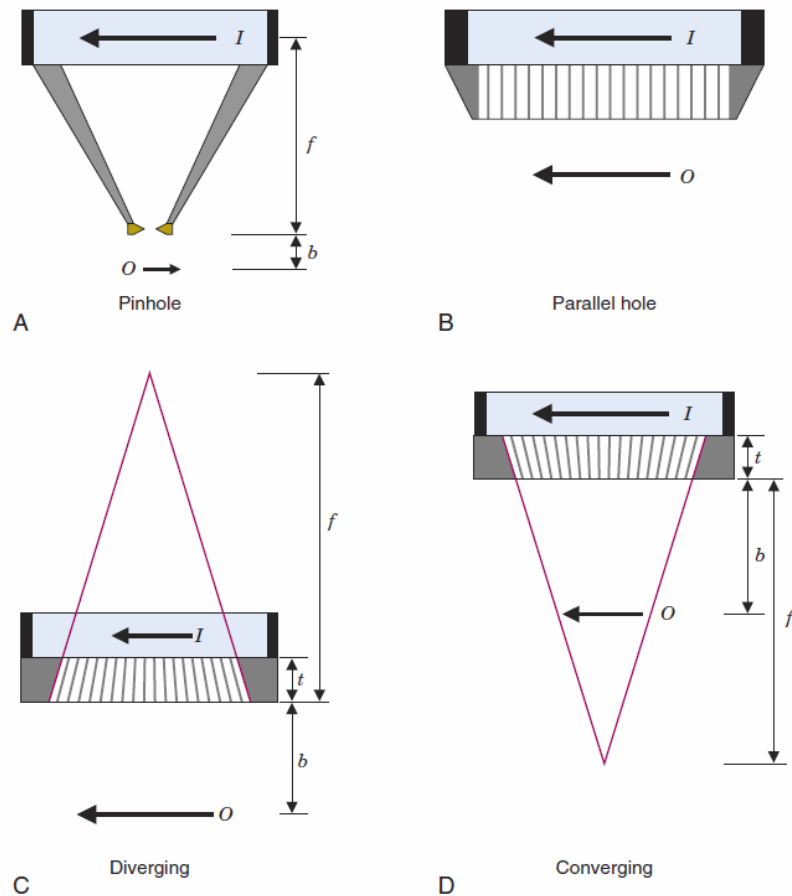
Figure 8 Different collimator types: A: pinhole collimator, B: parallel-hole collimator, C: diverging collimator and D: converging collimator.

Cherry et al., 2012 in Physics in Nuclear Medicine p.202.

noninverted, minified image of the source distribution. A diverging collimator is used for imaging of large organs on a small detector, such as the liver.

In the converging collimator (see *Figure 8 D*), the holes are shaped in such a manner that they converge to a point approximately 40-50 centimeter in front of the collimator. This causes a noninverted magnification of an object positioned between the converging point and the collimator face. The reason for such collimators is to utilize the whole detector surface of a large detector for imaging of small organs.

2.4.3 Event detection

A gamma camera may detect four different types of events during an examination, as shown in *Figure 9*. Only one event provides correct positional information. In the following, the four event types are described for a gamma camera with a parallel-hole collimator.
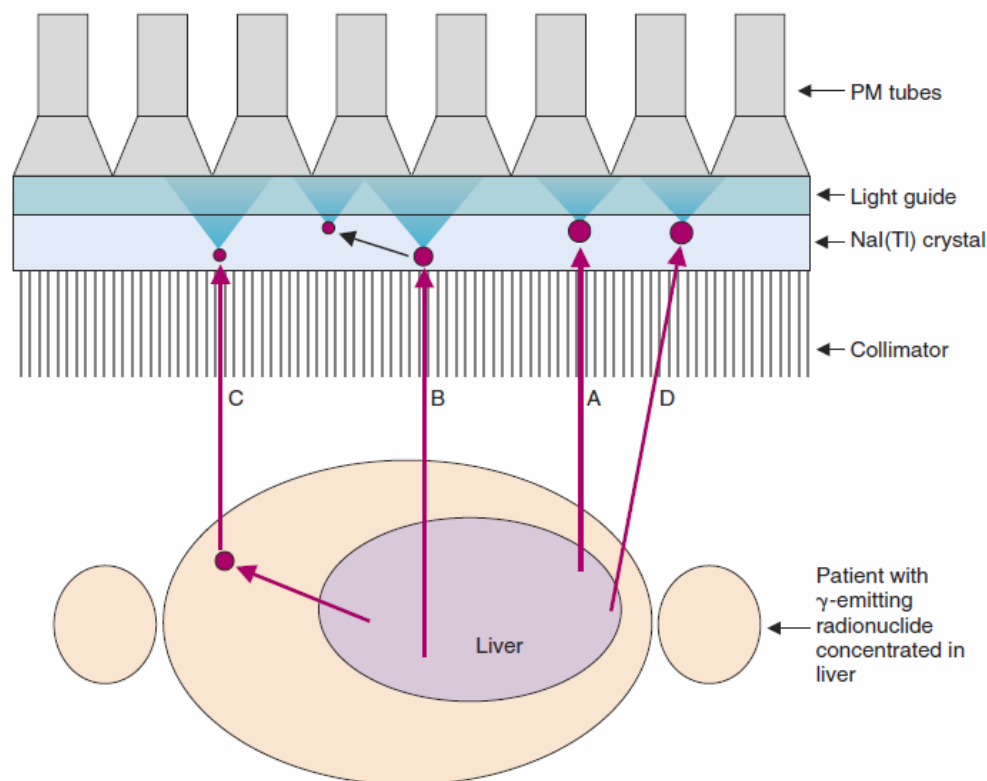
Figure 9 Four different event types that may be detected by a gamma camera. The red dots show locations of γ-ray interactions. A: valid event, B: detector scatter event, C: object scatter event and D: septal penetration.

Cherry et al., 2012 in Physics in Nuclear Medicine p.205.

Valid event: A γ-ray is emitted parallel to the collimator holes and reaches the NaI(Tl) crystal. All of its energy is deposited at a single location by interaction via the photoelectric effect (see *Figure 9 A*).

Detector scatter event: a γ-ray is emitted parallel to the collimator holes but interacts with the NaI(Tl) crystal via Compton scattering (see *Figure 9 B*). The scattered γ-ray can interact again with the NaI(Tl) crystal, in which case, the all of the energy is deposited in the crystal. This causes a mispositioning of the event between the two interaction locations, since energy discrimination cannot be used to reject this event. If the scattered γ-ray escapes the detector only a part of the energy is deposited in the detector. It is likely that the event is rejected due to the energy discrimination. The detector scatter event occurs very rarely.

Object scatter event: a γ-ray interacts by Compton scattering within the object and passes afterwards the collimator an reaches the NaI(Tl) crystal (see *Figure 9 C*). Sometimes the event is then detected many centimeters from the primary emission,

which leads to a mispositioning of the event and so to a low-spatial-frequency background and a loss of contrast in the image. During this process, the γ-ray loses energy, which leads to a smaller signal at the detector. It is likely that some of these events are rejected due to energy discrimination.

Septal penetration: A γ-ray reaches the NaI(Tl) crystal without having a parallel emission direction as the collimator holes. This is possible, because there is a small chance that the γ-ray penetrates the thin lead walls of the collimator, which results again in blurring of the image (see *Figure 9 D*). This event becomes increasingly important when applying high-energy γ emitter or collimators with very thin septa.

2.4.4 Event localization

The event localization is described in the following by a one-dimensional example (see *Figure 10*). A γ-ray interacts with the NaI(Tl) detector crystal by photoelectric effect and feeds light to two PM. They receive a different amount of light, as it is illustrated in *Figure 10*. If the relation between the signal amplitude and the location of the event with respect to the center of the PM is linear, then the following equation can be applied:

$$S_1 D_1 = S_2 D_2 \qquad (1)$$

And

$$D = D_1 + D_2 \qquad (2)$$

gives the following equations for the distances:

$$D_1 = \frac{S_2 D}{S_1 + S_2} \qquad (3)$$

$$D_2 = \frac{S_1 D}{S_1 + S_2} \qquad (4)$$

With the linear assumption, mentioned above, the distances D_1 and D_2 can be calculated easily. However in reality, the signal is not linear, thus corrections, such as calibration for spatial nonlinearity, have to be applied.
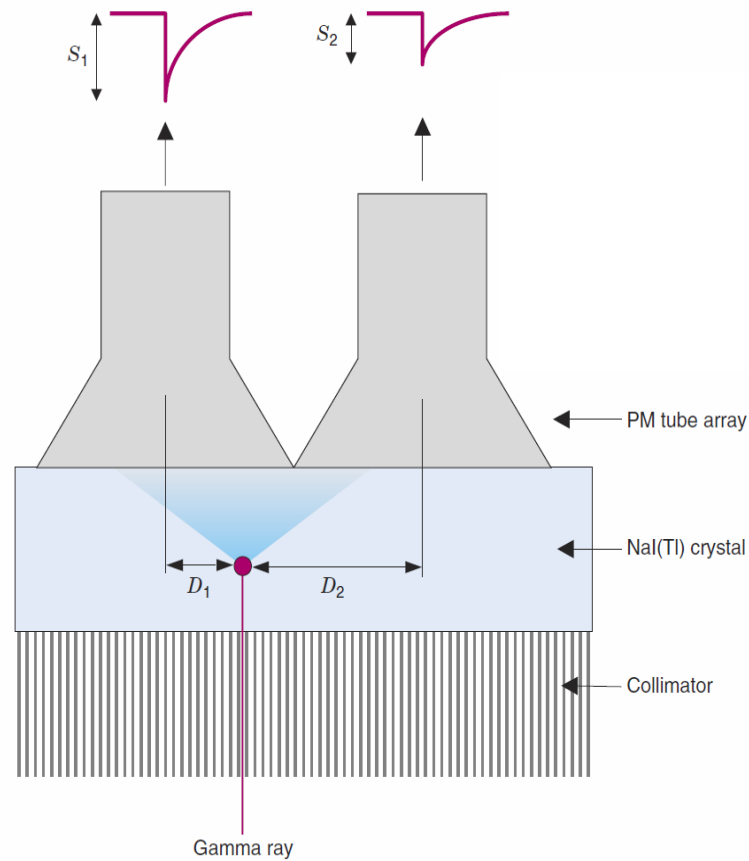
Figure 10 Illustration how the event is localized by light sharing between two PM tubes

Cherry et al., 2012 in Physics in Nuclear Medicine p.199.

2.4.5 Single Photon Emission Computed Tomography

A gamma camera, located at a fixed position, is able to generate a two-dimensional image from the original source distribution. By rotating the camera around the patient, multiple images from different angles at equally spaced angular intervals can be created (see *Figure 11*). This can be achieved by mounting the gamma camera on a rotating gantry. The result is a stack of one-dimensional projection data, which are used to reconstruct a cross-sectional two-dimensional image of a certain position along the patient axis (z-axis).

The combination of many two-dimensional images from different positions along the patient axis, allows the formation of a three-dimensional images volume. This method of tomography with emission of single or multiple γ-rays with no angular correlation, is called Single Photon Emission Computed Tomography. For clinical purposes, usually matrices of 64x64 or 128x128 and 64 to 128 projection views per rotation are used for reconstruction. In principle, also a half rotation of the gamma camera is enough to
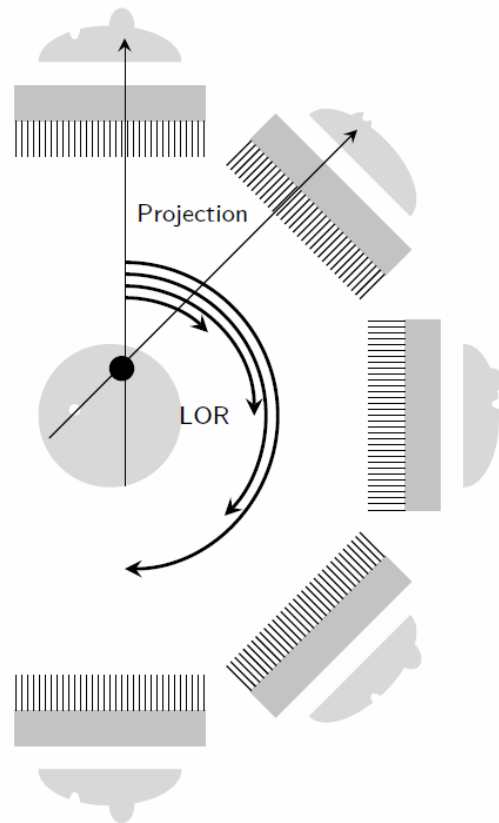
Figure 11 SPECT principle of a rotating gamma camera around the patient.

Courtesy of A. Hirtl.

reconstruct an image. Some SPECT devices have two or more detector heads rotating around the patient. These systems allow to record twice or more projections simultaneously per rotation, reducing the overall examination time or in an increased data set. The projection data from the source in X-Y coordinates are usually stored in a new coordinate system with two variables s and φ, also known as sinogram (see *Figure 21* and *Figure 22*). In Chapter 2.5.4 the sinogram will be presented again in combination with PET in more detail.

Quality control

Quality control (QC) of SPECT devices are recommended by international organizations [50] prior to clinical use and should be performed on a regular basis. Thus, quantitative validation of tomographic imaging properties, i.e. spatial resolution, contrast and inhomogeneity are crucial for the total performance of a SPECT system. The modular Jaszczak phantom (see *Figure 12*) has proven to be a valid test device and is commonly used for that purpose. It consists of cold rods for sector contrast (spatial resolution), cold spheres (for sphere contrast) and a homogeneous cylinder for inhomogeneity (ring artefacts) [51].
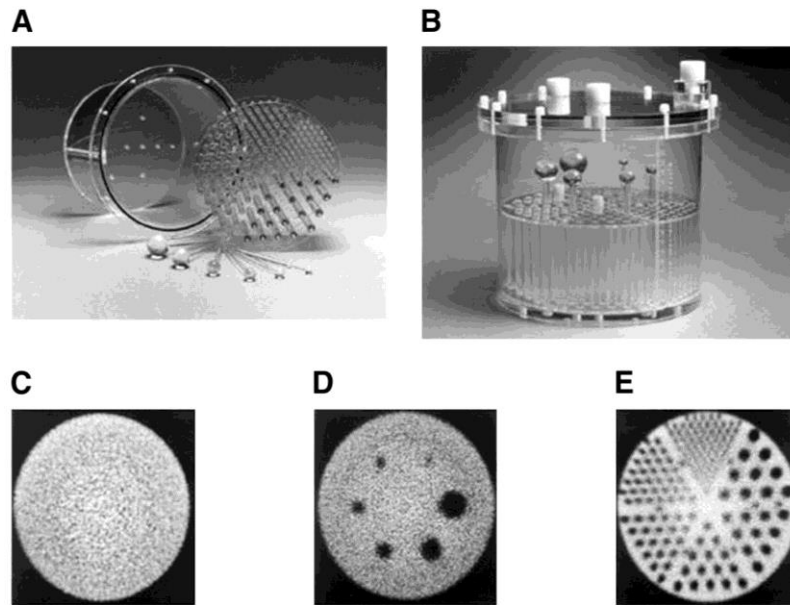
Figure 12 Image of a Jaszczak phantom. A: Disassembled Jaszczak phantom, B: phantom (Deluxe Jaszczak Phantom; Data Spectrum Corp.), C: plain section for evaluation of tomographic uniformity, D: cold-sphere part for evaluation of sphere contrast, E: cold-rods section for the evaluation of spatial resolution.

Pat Zanzonico J Nucl Med 2008;49:1114-1131

Ring artefacts in the reconstructed image can occur due to nonunifomities in the detector at the time of scanning. The artefact appears in the reconstructed image as ring shape due to the fact, that the detector head, containing all the detector units, is rotated $360°$ around the patient or phantom. QC with phantoms are usually performed in order to detect these artefacts [52].

2.5 PET

2.5.1 General concept of radionuclide imaging in PET

Positron emission tomography (PET) is an imaging technique in nuclear medicine that produces a three-dimensional image of biochemical and physiological functions in a living organism. A positron-emitting radionuclide (tracer) linked to a biologically active molecule is injected into the body. After the decay, the positron annihilates almost instantly with an electron, resulting in the emission of two photons in opposite directions. The simultaneously emission of the two photons back to back is the basis of coincidence detection and coincidence imaging [53].

2.5.2 System Components

In comparison to SPECT, PET consists of an entire ring of detector units and no collimator, because the different modality makes it dispensable. The detection principle is basically similar used in SPECT (see *Figure 13*). However, in PET the detector units are arranged in a block design (see *Figure 14*), i.e. a large piece of scintillator crystal is segmented into several smaller elements. In this design four PMTs are used to read out multiple detector units, resulting in an increase in intrinsic resolution at low costs, since PMTs are very expensive [54]. By combining the signals from a four-PMT array the determination of the segment in which a photon is detected can be calculated (see *Equation 5 and Equation 6*).

$$X = \frac{(B - A) + (D - C)}{A + B + C + D} \qquad (5)$$

$$Z = \frac{(C - A) + (D - B)}{A + B + C + D} \qquad (6)$$

A, B, C, D … signal from PMTs
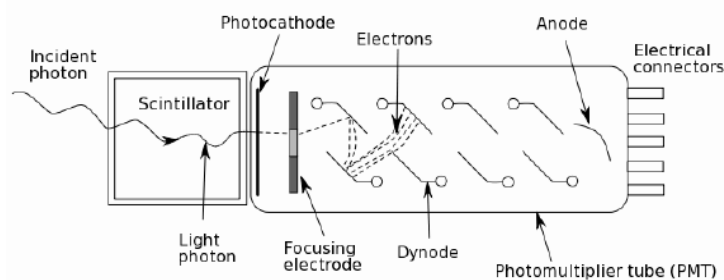
Figure 13 Illustration of a single PET detector unit consisting of the scintillator crystal and the photomultiplier.

http://nuit-blanche.blogspot.co.at/2010_07_01_archive.html
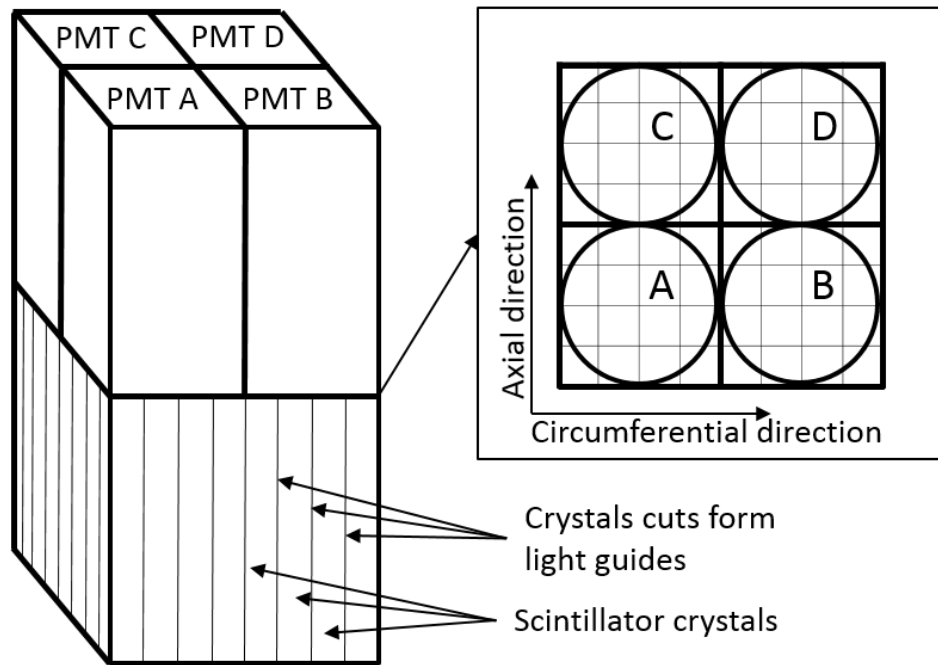
Figure 14 Block detector design used in PET.

2.5.3 Physical background

PET imaging is based on the positron decay followed by the annihilation process with an electron and the emission of two photons emitted back-to-back [53]. The positron is the antimatter of the electron and has the same mass as the electron but a positive rather than a negative charge [55]. In *Equation 7* the positron decay is described:

$$\ _{Z}^{A}X_{N} \ \rightarrow \ _{Z-1}^{A}Y_{N+1} + \ e^{+} + \ \upsilon. \qquad\qquad (7)$$
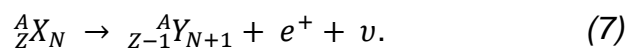
A proton from the nucleus is converted to a neutron. In addition, a positron and an electron-neutrino are emitted. During this decay the nuclide becomes a new nuclide due to the change of the proton number.

The interaction of the electrically neutral and very light neutrino with other particles is very weak and thus not relevant in nuclear medicine. Yet it is responsible for the variable energy of the positron in the positron decay. In comparison, gamma emissions have fixed energies for given radionuclides [55].

Positron decay is predominant in proton-rich nuclides. Isotopes like 18F, 13N, 11C and 15O are the most commonly used radionuclides for PET imaging. Interestingly these elements appear frequently in the human body. Their isotopes have the same chemical

properties, so the human body cannot distinguish them from each other, which makes them excellent tracers. Another advantage is the short half time of these radionuclides [53].

Positrons passing through matter lose energy just like electrons. This loss is caused by ionization and excitation of adjacent atoms and molecules. After a few millimeters the positron has lost enough energy and annihilates with an adjacent electron. *Equation 8* describes the annihilation process, where the positron collides with an electron, which represents its antiparticle:

$$e^+ + e^- \rightarrow \gamma + \gamma. \qquad\qquad (8)$$

The total energy of a particle can be divided by its mass and its energy of motion. When a positron interacts with an electron only their masses contribute to the initial energy and their energy of motion is neglected due to the relatively slow movement. Their energy is then converted into the combined energy of the 2 photons. Those two photons are emitted each with an energy of exactly 511 keV back-to-back, due to conservation of energy and momentum. The energy of each photon is determined by its mass multiplied with the speed of light squared (see *Equation 9*) and results in:

$$E_\gamma = m_e * c^2 = 511 keV. \qquad\qquad (9)$$

2.5.4 Event detection

In a PET-scanner the simultaneous emission of two photons back-to-back is used for detection and imaging. The detection unit is formed by a ring of radiation detectors located around the patient (see Figure 15). The detection of two photons at the detector ring within certain time period is called "coincidence". This time period is termed coincidence time window and is calculated as followed:

$$2\tau \geq |t_1 - t_2| \qquad\qquad (10)$$

$t_1 \ldots$ *time, where detector one is hit*

$t_2 \ldots$ *time, where detector two is hit.*

The system counts the event, if two signals are detected within this coincidence time window, others are discarded (see *Figure 16*). The coincidence indicates that an annihilation process happened somewhere along the line between two detector units.
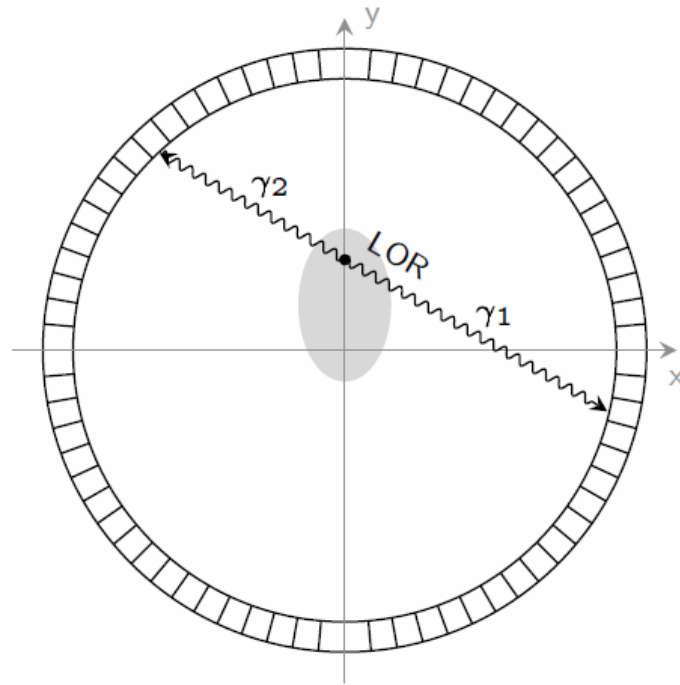
Figure 15 Illustration of a PET device. The patient is located in the center of the PET. Within the patient a positron emission occurs and two photons are emitted back-to-back towards the detector ring. The line between the two detector units being hit are called Line of response (LOR).

Courtesy of A.Hirtl.

This path between two detector units is termed line of response (LOR). Multiple coincidence events occurring between detectors express the amount of radioactivity located on the LOR. Considering a detector ring consisting of n detectors, each pair of detectors describes a potential emission path, resulting in n^2/2 ways to pair up. During a PET scan, the system is recording how often each pair of detectors is hit in coincidence.
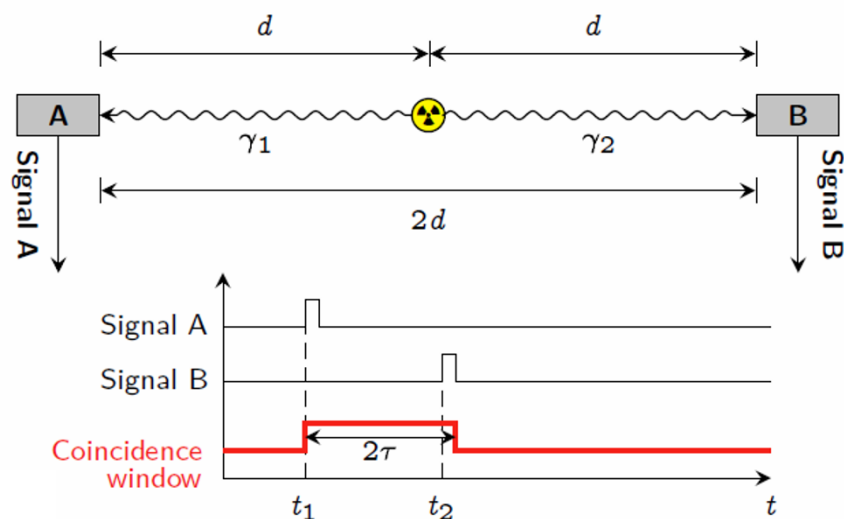
Figure 16 Coincidence time window.

Courtesy of A. Hirtl.

During a PET measurement several events can occur, such as a single event, a true coincidence, a random coincidence, multiple events and scattered events. They are briefly described in the following paragraphs:

Singe event: If just a single photon is counted by a detector the event is called single event. This can be caused by attenuation or scatter of one of the two annihilation photons, resulting in a deflection or even a stop (see *Figure 17*). Hitting only one detector means that no LOR can be assigned. Attenuations cause an overall loss of counts, which results in increased noise and inaccurate quantization of radioactivity distribution.

True coincidence: If two photons originated from the same annihilation event are counted by two opposite detectors within the coincidence time window, then this event is termed true coincidence (see *Figure 19 A*).

Scattered event: If one or both of the annihilation photons undergo Compton scattering and are detected within the coincidence time window, the event is called scattered event (see *Figure 19 B*). Scattered photons experience a loss of energy and a change of their direction. But since most PET detectors have a relatively poor energy resolution, those photons cannot be discriminated. The consequence is the assignment of LORs, which are not correlated to the actual annihilation event, leading to a decreased image contrast. In *Figure 18 A* the source of radiation appears even to
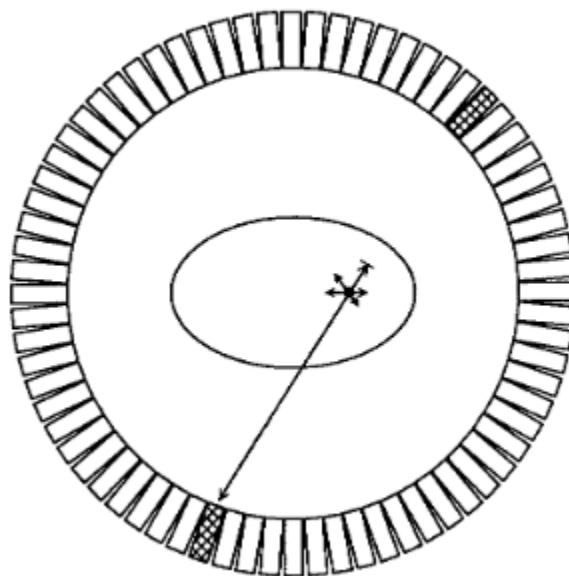
Figure 17 Single event, due to attenuation of an annihilation photon.

Turkington, T.G., *Introduction to PET Instrumentation.* Journal of Nuclear Medicine Technology, 2001. 29(1): p. 6.
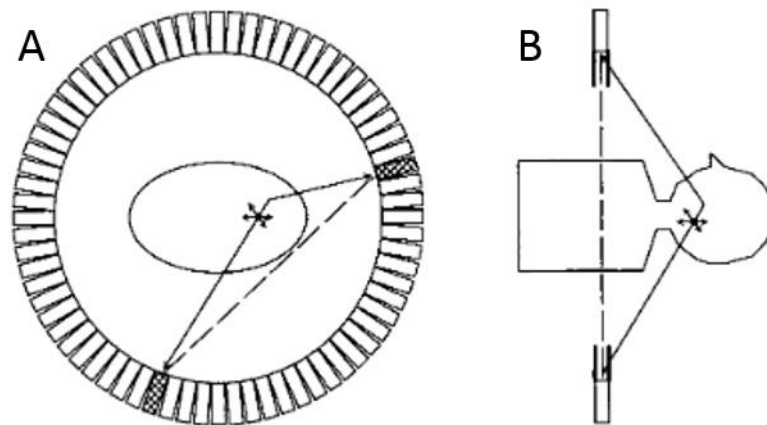
Figure 18 Scattered events at PET.

Turkington, T.G., *Introduction to PET Instrumentation.* Journal of Nuclear Medicine Technology, 2001. 29(1): p. 6.

be outside of the patient. Another possibility is that the annihilation occurs outside the plane of the detector ring (see *Figure 18 B)* but appears to be inside the body due to scatter events. In the case of out-of-plane scatter, shields are used to block radiation coming from outside the field of view (FOV) of the ring.

Random coincidence: Considering two annihilation events occur and four photons are created during this process. Further, two of those photons from different annihilation events reach the detector within the coincidence time window. This coincidence is counted by the system although the photons involved derived from different annihilation positions, leading to a wrong LOR and therefore to a wrong activity distribution (see *Figure 19 C*). This event is highly dependent on the number of decays per second.

Multiple events: This event is similar to the random coincidence events except that three hits are counted at the detector ring within the coincidence time window (see *Figure 19 D*). The system cannot assign the correct LOR. Therefore, these events are discarded.

The prompt count rate consists of the true coincidences, the random coincidences and the scattered events. These events are counted by the PET-system.
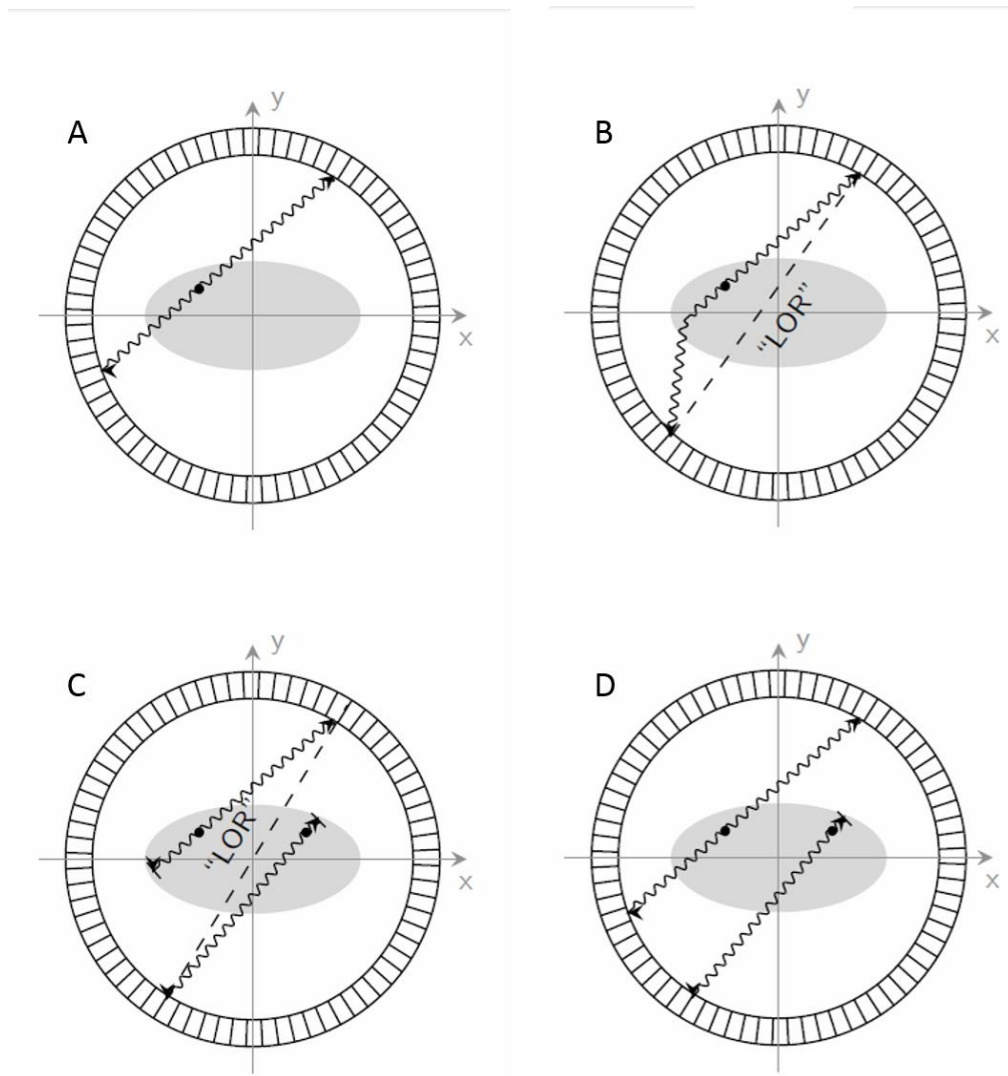
Figure 19 Possible events that may occur during PET. A: true coincidence, B: scattered events, C: random coincidences and D: multiple events.

Courtesy of A. Hirtl.

2.5.5 Event localization

Assuming a patient with a small tumor is undergoing imaging in a PET scanner consisting of a single ring detector. *Figure 20 A* illustrates the patient's head within the PET scanner. A positron emitting radiopharmaceutical is injected into the patient. This agent will preferentially go to the tumor site, where it will decay by emitting a positron. A black circle marks the position with a high uptake from the radiopharmaceutical. After travelling for a short distance the positron recombines with an electron by annihilation, leading to a coincidence detection, which is described by the LOR. This LOR can be parametrized and plotted in a diagram by its angle of orientation φ and the shortest distance s between the LOR and the center of the gantry (see *Figure 20 B*)[56].
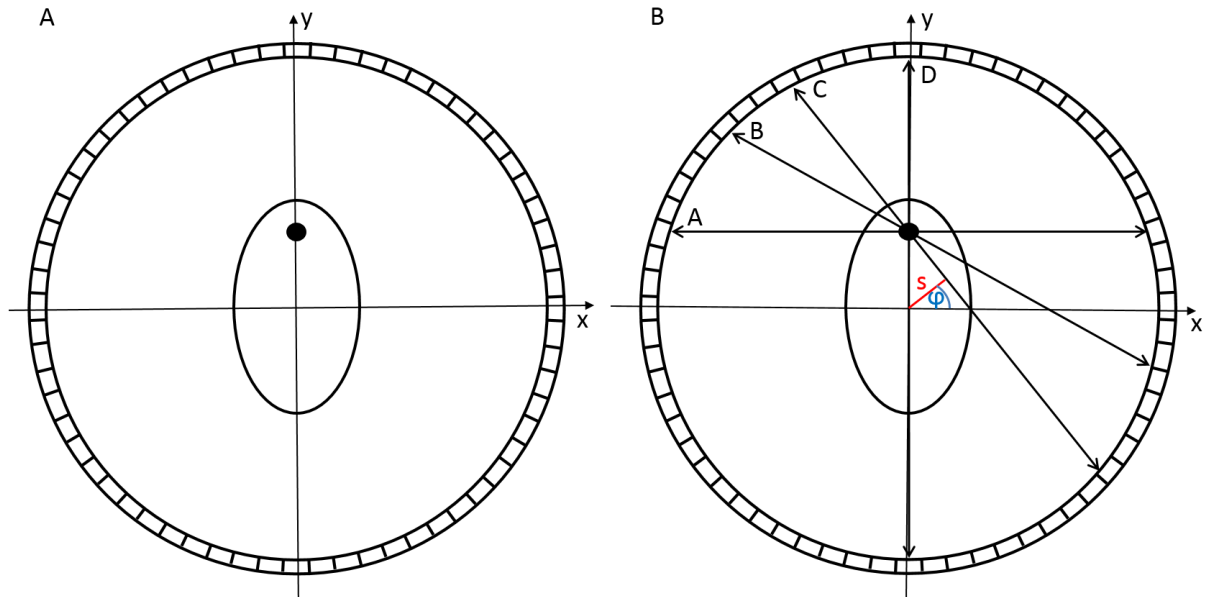
Figure 20 Illustration of a Patient's head in a PET scanner. Four LORs from a mutual origin are presented with different angles.

$$\begin{pmatrix} x \\ y \end{pmatrix} \cdot \begin{pmatrix} \cos \varphi \\ \sin \varphi \end{pmatrix} = s \qquad (11)$$

Resulting in

$$x \cos \varphi + y \sin \varphi = s. \qquad (12)$$

Figure 20 B shows 4 different LOR's. They all originate from roughly the same location where the annihilation processes occur but have different angles and displacements to the center of the gantry. In *Figure 21* for all 4 LOR'S the angular orientation is plotted on the y-axis and the distance to the center of the gantry is plotted on the x-axis.

Plotting a high amount of LOR's from the same location of positron decay forms a graph, which looks like a sine wave. This graph is called sinogram. It contains all the information in order to determine the location of the tumor in the transverse plane. The angular orientation can be determined from the phase of the sine wave, while the displacement from the point to the center of the gantry can be determined from the amplitude of the sine wave [56].
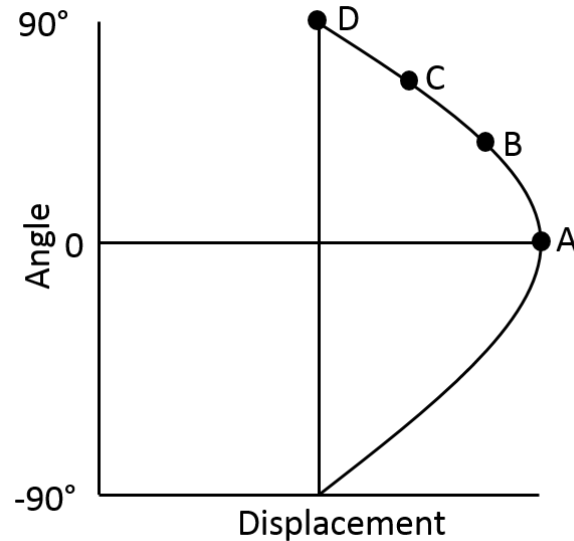
Figure 21 Four LORs plotted as a sinogram with their angular orientation and their displacement from the center of the gantry.

Moving from this simplified example to a more realistic object, a sinogram will consist of many pixels and cover a large number of overlapping sine waves. Each pixel in the sinogram corresponds to a LOR. The value of the pixel is described by the number of coincidence detections of that specific LOR. The resulting sinogram represents one slice according to the current position of the patient in the scanner. By shifting the patient through the PET scanner multiple sinograms are recorded and a separate sinogram is obtained for each slice in z-direction. Therefore a full multislice PET study from a body consists of a set of sinograms [56].

Figure 22 shows a PET slice through a patient's body as a sinogram and its associated transverse reconstruction. Each pixel value along a horizontal row in the sinogram represents the amount of all of the events acquired along parallel LOR's at the angle that correspond to that specific row. Typically the first row corresponds to the angle from vertical LORs. The following rows represent the following angles, which are slightly different from the previous ones. Finally, a whole sinogram represents a collection of parallel LOR sums at different angles ranging from 0° to an angular range of 180°. Each row can be seen as a projection along the angle related to the row of this slice.

In comparison to SPECT, where each projection image represents the data obtained at a certain projection angle across all slices, in a PET scan each sinogram represents
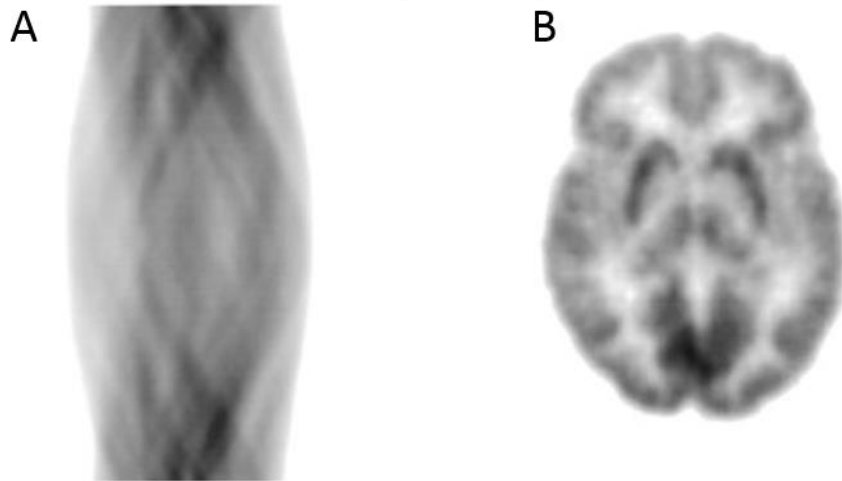
Figure 22 A: Sinogram of a brain and the corresponding transversal reconstruced image B.

Fahey, F.H., *Data Acquisition in PET Imaging.* Journal of Nuclear Medicine Technology, 2002. 30(2): p. 40.

the data collected for that slice across all projections angles. The computer can easily generate a series of projection views (similar to the raw data acquired in SPECT) from a set of sinograms from a complete multislice PET study. Therefore, raw PET data can be presented on the one hand as a series of sinograms with one sinogram for each slice, or on the other hand as a series of projection views for each projection angle [56].

As mentioned before, a row of a sinogram describes all coincidence events at a certain angle. Those coincidences are associated with parallel LORs. But due to the annular form of the detector, LOR's located in the center of the gantry are farther apart compared to VOI's near the periphery (see *Figure 23*). This variation in LOR spacing leads to errors in the reconstructed image especially for large objects and must be corrected by the so called "arc correction" due to the fact that the detectors are arranged on an arc [56].

Until now detectors were only in coincidence with detectors on the opposing side from the same detector ring. A PET scanner usually consists of multiple detector rings as is shown in *Figure 24*. If detectors from the same detector ring are in coincidence these events are called "direct coincidences". Thus, only detectors from ring one are in coincidence with detectors from the same ring, detectors from ring 2 only with detectors from ring 2 and so on. In this case the polar angle θ is zero and it is referred as 2d-mode (see *Figure 24*). A polar angle θ >0° implies the 3d-mode, which results in a higher slice sensitivity and an improvement in the axial sampling but increases scatter
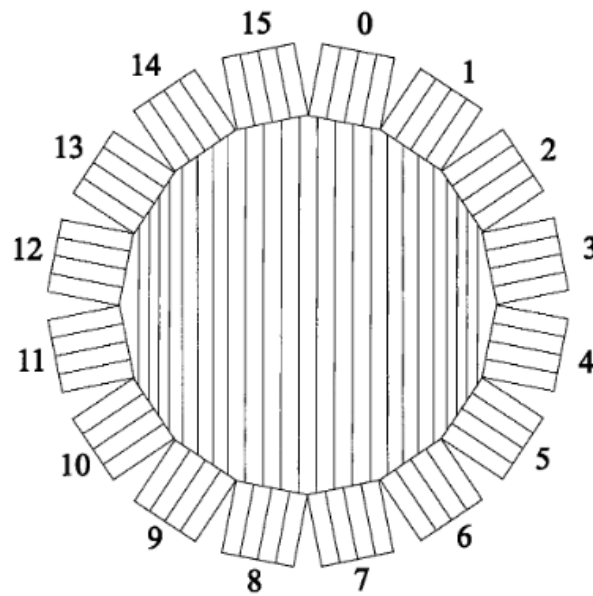
Figure 23 Arc correction for PET. The illustration shows all 90° LORs. Due to the arc-style of the gantry, LORs in the center are further away than those at the periphery.

Fahey, F.H., *Data Acquisition in PET Imaging.* Journal of Nuclear Medicine Technology, 2002. 30(2): p. 40.

events [54]. If this polar angle is opened, coincidence between detectors located on different rings are allowed. Those coincidences are termed "cross" coincidences. A way to define and illustrate the allowed coincidences within the different rings is the so-called Michelogram. Each ring is marked with a number. The detector ring on one side are listed on the x-axis, while the detector rings on the other side are listed on the y-axis. In *Figure 25* several modes are presented.
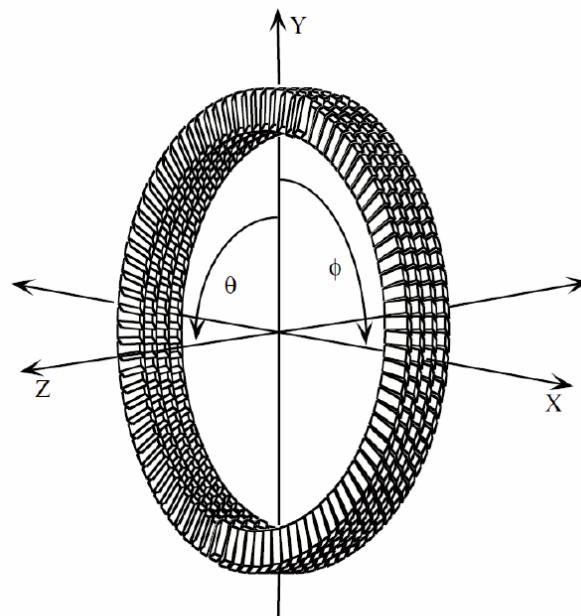
Figure 24 Illustration of a PET with multiple ring detectors.

Bailey et al., 2006, Chapter 3.
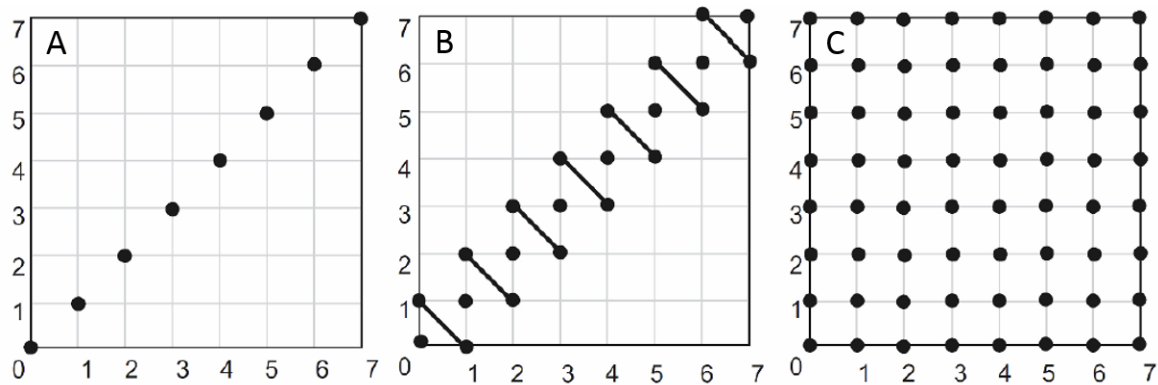
Figure 25 Michelogram of a 2D PET sapling. A: Direct planes only, represented as dots (plane 0 with 0, 1 with 1 ect. resulting in 8 sinograms. B: Interplanes with ± 1 are used and summed yielding to approximately twice the count rate $2N - 1 = 15$ sinograms. C: Full three dimensional acquisition. Each plane is stored separately resulting in 64 sinograms.

Bailey et al., 2006, Chapter 3.

2.5.6 Attenuation correction

Attenuation occurs when true coincidence events are lost due to their absorption within the body or due to their scattering out of the detector. The attenuation is calculated to:

$$I(x) = I_0 e^{-\mu_l x} \qquad (13)$$

$I(x)$ ...transmitted photon beam intensity

I_0 ... incident photon beam intensity

μ_l ... linear attenuation coefficient

The attenuation problem is greater with PET than in SPECT, because the average photon path distance from emission to detection is much longer in PET than in SPECT. The probability of attenuation is greater in the center of a body, thus, non-attenuation-corrected images present a diffusely lower level of activity in the center of the body compared to the body surface (see *Figure 26*). This loss of coincidence events can contribute up to 95% in PET imaging, particularly for larger persons, yielding to image noise, image distortion and image artifacts. Therefore, attenuation correction is of major importance for quantitative and qualitative nuclear imaging.

The idea for attenuation correction is to create an absorption pattern or transmission scan (see *Figure 27 B*), since absorption of LORs will always occur at the same
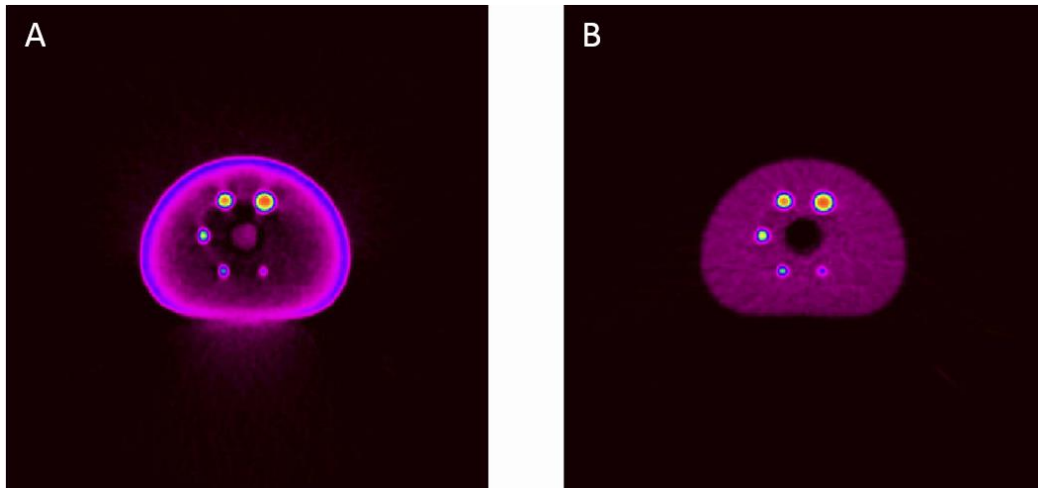
Figure 26 A: Non attenuation-corrected image. B: Attenuation corrected image.

Courtesy of B. Knäusl

location within the same patient without movement. In addition, a normalization scan, a so called blank scan (see *Figure 27 A*), is obtained from the empty PET-scanner. These to scans are used to calculate the attenuation accordingly:

$$A_{i,j} = \frac{Blank\ scan_{i,j}}{Transmission\ scan_{i,j}}.$$ (14)

$A_{i,j}$ … attenuation correction factor for detector pair (i,j)

The transmission scan can be obtain either by rotating ^{68}Ge-^{68}Ga rods or CT. In aPET/CT scanner the positron emitter is replaced by the CT. Attenuation correction can be achieved much faster with CT than with ^{68}Ge-^{68}Ga rods.
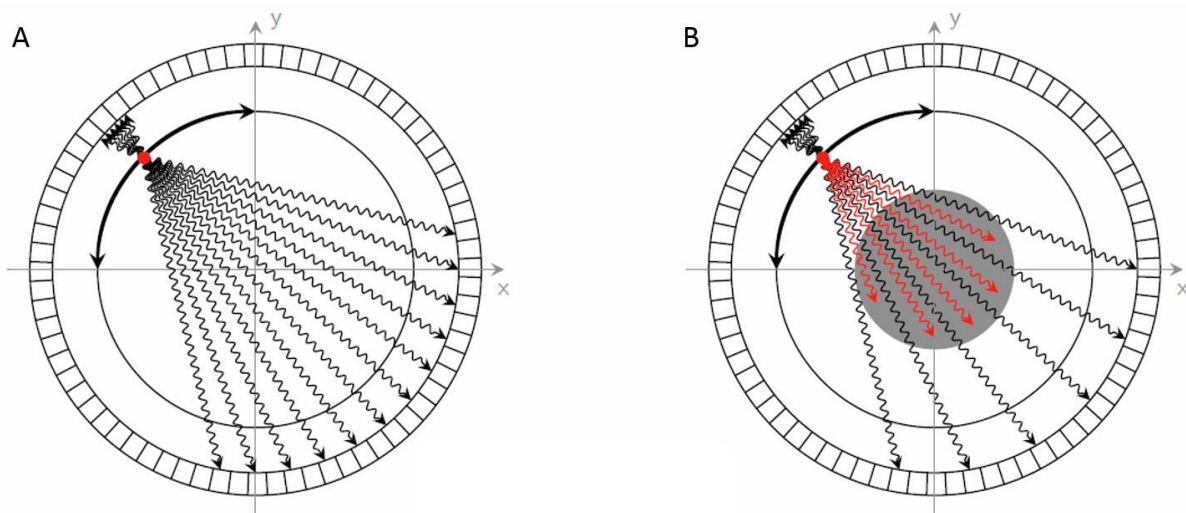
Figure 27 A: Illustration of the Blanc-scan and B: the Transmission-scan for the calculation of the attenuation correction factor.

Courtesy of A.Hirtl

2.5.7 Hybrid Imaging: PET/CT

The proposal to combine PET and computed Tomography (CT) was made in the early 1990s by Townsend, Nutt and co-workers. The idea was to incorporate a second imaging modality between the two banks of bismuth germinate detector blocks (BGO) of a PET-system (see *Figure 28 A)*. An oncologist suggested to add a CT in the gaps in order to provide anatomical information (see *Figure 28 B*). *Figure 28 C* shows a schematic of a possible arrangement of CT in the gaps between the PET detector blocks. However, the high density of x-ray components shown in *Figure 28 D* made the realization of the first hybrid PET/CT very challenging, due to the lack of space.

The goal was to develop a prototype composed of both clinical CT and clinical PET, which is able to acquire both data sets in a single scan session. Finally, in the late 1990s the first prototype PET/CT scanner became operational, by mounting a PET system on the rear of a spiral CT scanner. This approach solved the space problem, enabled the combined rotation of both components and the acquisition of CT and PET data sequentially, by moving the patient on the common patient bed from one imaging modality to the next. The combination of the functional images from PET and the anatomical images from CT is of major importance in diagnosis and staging of malignant diseases and detecting metastases. In addition, the CT images are used to generate the attenuation correction for the PET scan [57-59].

2.5.8 Standardized uptake value

The standardized uptake value (SUV) is a semiquantitative analysis used in PET/CT imaging to measure the rate and/or total amount of a tracer accumulation, such as 18F-fluorodeoxyglucose ([18F]-FDG) and 18F-Fluoroethylcholine ([18F]-FEC) in tumors. It describes the ratio of tissue radioactivity concentration at a position at time $C(t)$ and the injected radioactivity dose per kilogram of the patient's body weight (see Equation 15). The amount of injected tracer and the patient size are the two variables, which vary in practice the most. This quantitative value of the uptake allows the comparison with other images [60].

$$SUV = \frac{C(t)\ [MBq/ml]}{injected\ activity\ [MBq]\ /\ body\ weight\ [kg]} \qquad (15)$$
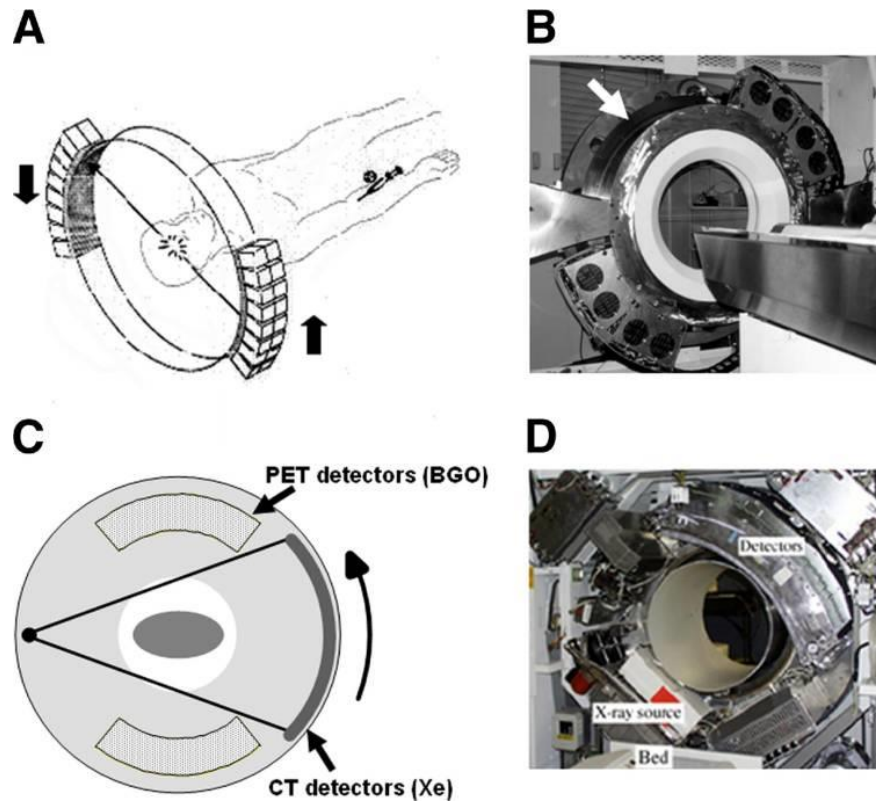
Figure 28 The first concept of a hybrid imaging technique composed of PET and CT. A: PET with two banks of bismuth germinate detector blocks (BGO). B: the gaps between the two banks allowed the insertion of a second imaging modality. C: Illustration of a possible combination of PET and CT. D: Photo of a typical CT scanner demonstrating that the suggestion in C is not really feasible due to the density of the x-ray components.

Townsend, D.W., *Combined PET/CT: the historical perspective.* Seminars in ultrasound, CT, and MR, 2008. 29(4): p. 232-235

3 Materials and Methods

This section describes the methods used in this study for the volumetric analysis. Before that, general information of the patients, their data, and the software used in this thesis are presented.

3.1 General

In this study, data from 24 Patients with HCC are investigated. The study was accepted by the ethic committee in in Munich in October 2014. Patients gave their written informed consent. Each patient was diagnosed with HCC in the BCLC stage B but without any metastasis. They underwent a pre-FEC examination (FEC-PET/CT) and a MAA-evaluation (MAA-SPECT), followed by the SIRT-Therapy a few weeks later. After several weeks one or more post FEC examinations were performed. All these clinical examinations were performed in Munich (Klinikum der Universität München, Campus Großhadern) between 2009 and 2012.

3.2 Patients

The majority of the patient suffered from multifocal HCC associated with chronic HCV. One patient had HCC associated with HBV. Three Patients exhibited recurrent HCC, one of them in the transplanted liver. The birth dates ranged from 1929 to 1958 except for one patient who was born in 1985. The patients investigated in this study deceased between 2011 and 2014 due to their severe disease.

3.3 Data and software

For the determination of the metabolic volume, the vascularization volume and ultimately their intersection, both data sets from FEC-PET/CT and MAA-SPECT from each patient are used and analyzed with a three-dimensional imaging software (HERMES HYBRID 3D). This software displays the recorded FEC-PET/CT and MAA-SPECT images from the patients in transversal, coronal and sagittal views. The determination of the volumes can be achieved either manually, by drawing the volume contours on several slices and approximate them for 3D, or by setting a threshold value and sum all regions above that value to a volume of interest (VOI).

The data for the determination of the metabolic volumes (PET-CT) were attenuation corrected, allowing the usage of SUV-values. In contrary, for the determination of the

vascularization volume only gray-values can be used, since the MAA-SPECT data were not quantified according to the SUV.

The CT part of the FEC-PET/CT was used as a coordinate system and reference point. In order to use the same coordinate system the MAA-SPECT was registered to the CT part of the FEC-PET/CT scan. This co-registration of the MAA-SPECT images to FEC-PET/CT images was performed manually with the HERMES-Software and supervised by medical doctors. These calculated volumes can be saved as VOIs (region of interest) and can be further processed.

The results from the volumetric analysis are compared with the survival data of the patients using statistical programs (SPSS). The Results are presented in ROC-analyses and Kaplan-Meier estimations.

3.4 Volumetric analysis

The determination of the liver volumes are described in details in the following subchapters.

3.4.1 Total liver volume

The FEC-PET/CT scan is used for the determination of the whole liver volume of the patient (see Figure 29). The CT scan provides a good visibility of the organ and its boundaries and is therefore appropriate for the volume estimation. Moving along the z-axis grants the view of the transversal plane. The first step is to locate the upper (or lower) contour of the liver. At the slice, where the liver appears for the first time, the contour of the liver is drawn manually with the tool "add VOI". Then the following slice is selected and the next VOI is set, describing the liver boundary. This process is repeated until the lower (upper) end of the organ is reached. The "approximation" tool estimates the whole volume by approximating the VOIs drawn in the transversal plane along the z-axis. It is recommended to use also to the coronal and the sagittal view in order to correct the determined volume from potential errors simply by adding or deleting VOI segments. In addition, the PET part is also very valuable to verify the outcome from the volume determination. The final VOI, representing the total liver
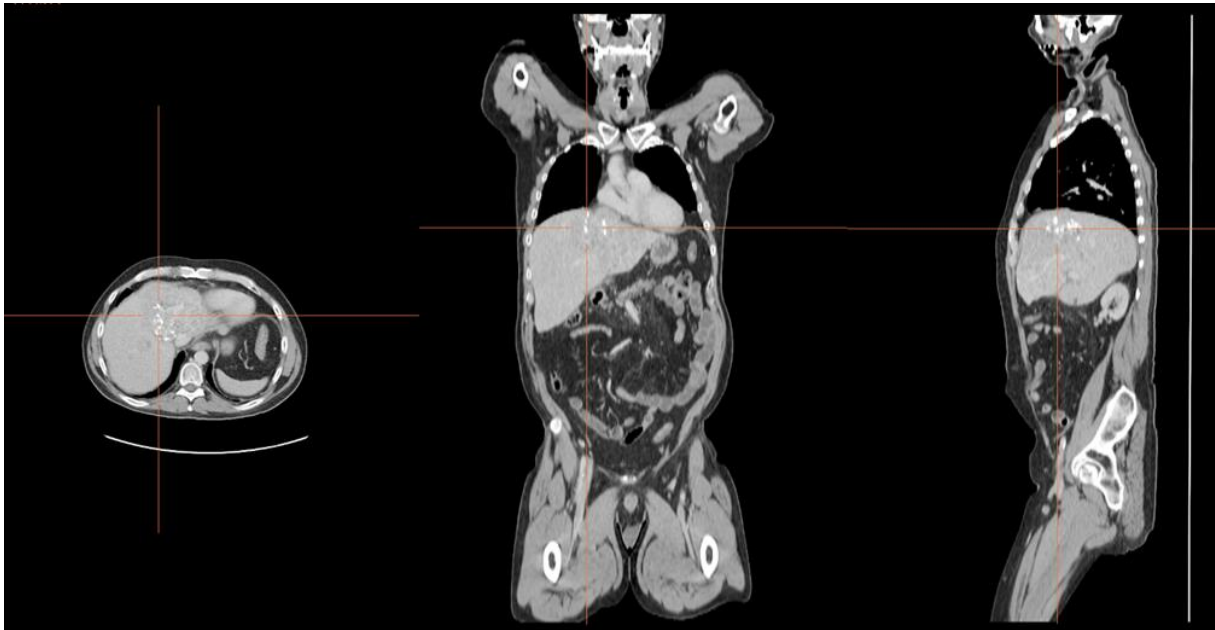
Figure 29 CT-image of a patient for the estimation of the total liver volume in the transverse, coronal and sagittal view (from left to right)

volume, is then saved and used afterwards to calculate the intersections with the metabolic tumor volume and the vascularization volume.

3.4.2 Vascularization volume

For the determination of the vascularization volume the MAA-SPECT scan is used (see *Figure 30 A*). First of all, the MAA scan must be co-registered to the CT scan from the FEC-PET-CT scan, so that the anatomic structure overlaps. This might be challenging, due to the fact that the MAA scan is often heavily shifted and shows no clear liver contours but only the blurred 99mTc uptake (see *Figure 30 B*). The MAA scan has a much lower spatial resolution compared to PET. The importance of this task becomes clear when the intersection of the metabolic tumor volume and the vascularization volume is determined. A small shift of the MAA-scan will change the intersection volume dramatically. Therefore, the co-registration is done carefully and supervised by medical doctors.

After the two scans are aligned (see *Figure 30 C*) a reference voxel is placed in a liver area assumed to be healthy. The MAA scan shows the distribution of 99mTc microspheres in the liver, which are injected into the tumor vessels through the liver artery. In the MAA scan there are no SUV values but intensity distributions displayed as shades of gray. The threshold for the VOI, which represents the vascularization volume, is defined as 200% of the maximum value found in the reference voxel. All
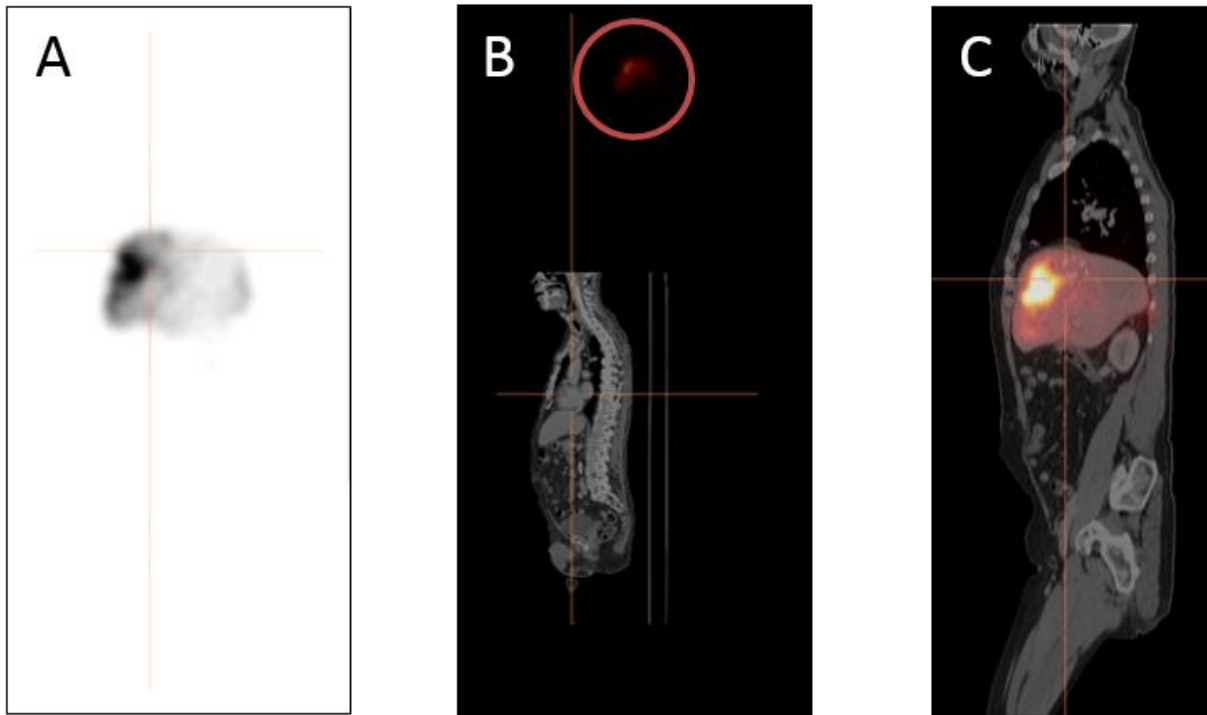
Figure 30 A: Sagittal SPECT-image without CT. B: When assembled with CT-image the SPECT image is shifted and must be registrated before analysis can be performed. C: SPECT-image is successfully registrated with CT-image.

liver regions with values above that threshold value are considered highly perfused with oxygen-rich blood and are added to the blood-perfusion-volume-VOI (MAA-volume).

This first determined VOI in this analysis is termed uncorrected blood-perfusion-volume because some uptakes may come from regions outside the liver. Therefore, the intersection of the uncorrected vascularization volume and the total liver volume is determined by the "AND" function. The resulting VOI is called the corrected blood-perfusion-volume and represents only regions within the liver with high vascularization compared to the normal, healthy liver tissue.

3.4.3 Metabolic tumor volume

The metabolic tumor volume is determined from the FEC-PET-CT scan. It sometimes occurs that the PET-image is shifted to the corresponding CT-image, due to motion artifacts from respiration (see *Figure 31 A*). Therefore, the PET-image must be registered correctly to the CT-image before starting analysis.

Choline is an important component for the biosynthesis of cell membranes in the liver and when labeled with 18F an excellent tracer for HCC with a high specificity [61]. After
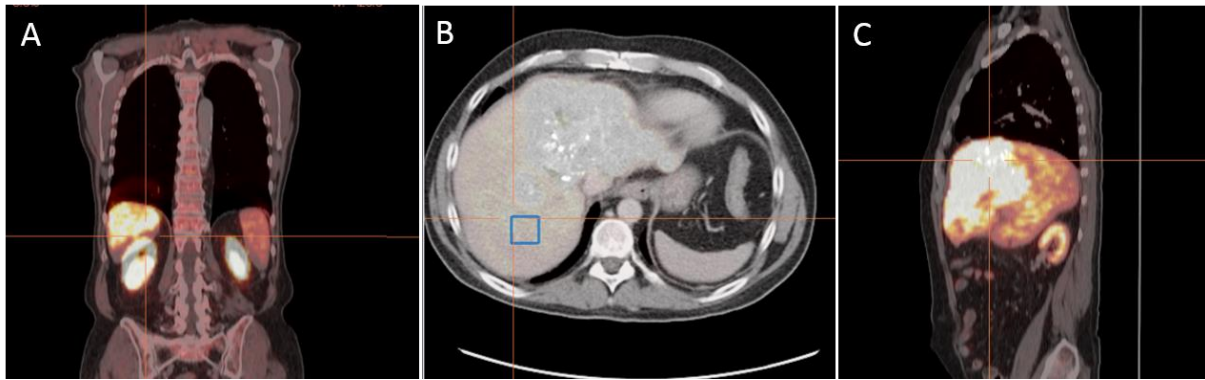
Figure 31 A: Shift between PET-image and CT-image, due to motion artifacts, e.g. breathing. B: Reference voxel for the determination of the threshold value set in a liver region assumed without tumorous tissue. C: Kidneys are also loaded with choline and must be removed from the threshold volume in order to get the corrected FEC-volume.

injecting the tracer into the patient, the radiopharmacon accumulates preferentially at HCC due to the high metabolic demand of the latter. Therefore, a high uptake of choline attached to 18F is expected in cancerous areas.

In order to define a threshold above which a malignancy can be assumed, a voxel is placed in an area where no tumor is expected (see *Figure 31 B*). This voxel represents a reference value for the normal, healthy liver tissue. The value of the SUV_{peak} , which represents the highest SUV-value in that voxel is used to determine the threshold. The threshold for the metabolic tumor volume in this thesis is 125% of the SUV_{peak} value. This value was chosen by medical doctors, clinical experience and for standardization purposes. The choice of this rather high value is due to the fact that the liver is often heterogenic in its morphology. Areas with SUV values above 125% of the SUV_{peak} from the reference voxel are defined as HCC.

The volume is then determined by using the "VOI threshold" tool. The Hybrid 3D program selects all areas with SUV values above the specified threshold and sums them up into a VOI. This is called the uncorrected metabolic tumor volume because there could be areas, which are selected but are not part of the liver, e.g. kidneys which have also a high uptake (see *Figure 31 C*). Therefore, the intersection of the total liver volume and the uncorrected metabolic tumor volume is determined (by the AND function), resulting in the corrected metabolic tumor volume where uptake outside the liver is neglected. Again, the VOI is saved and used later on for the comparison with the vascularization volume.

3.4.4 Intersection volume

The final step is the determination of the intersection volume (see *Figure 32*). For that matter, the two VOIs presenting vascularization volume and metabolic tumor volume are combined with the HERMES image tool "and". *In Figure 33 A* the single VOIs are shown in transverse, coronal and sagittal view for different colors. The VOI representing the vascularization is marked green, while the VOI illustrating the metabolic volume is marked blue.

The result intersection volume is a VOI representing sections, which are highly perfused with oxygen-rich blood and display a high metabolism compared to the surrounding liver tissue. This VOI is marked red in *Figure 33 B* in transverse, coronal and sagittal view.
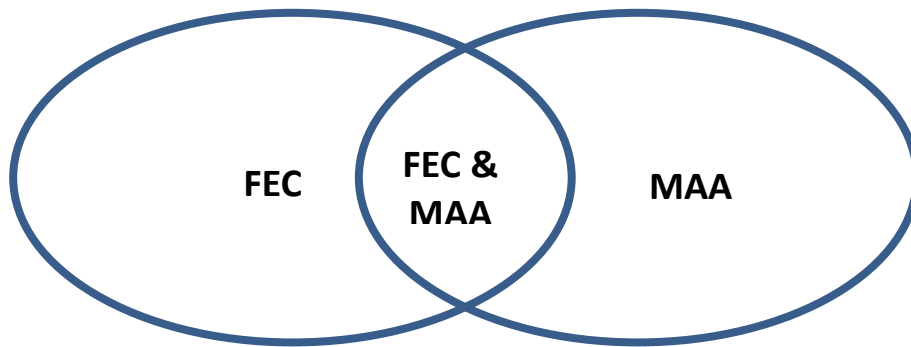
Figure 32 Schematic illustration of the Intersection volume consisting of regions with higher metabolic rate and elevated vascularization than the surrounding liver tissue.
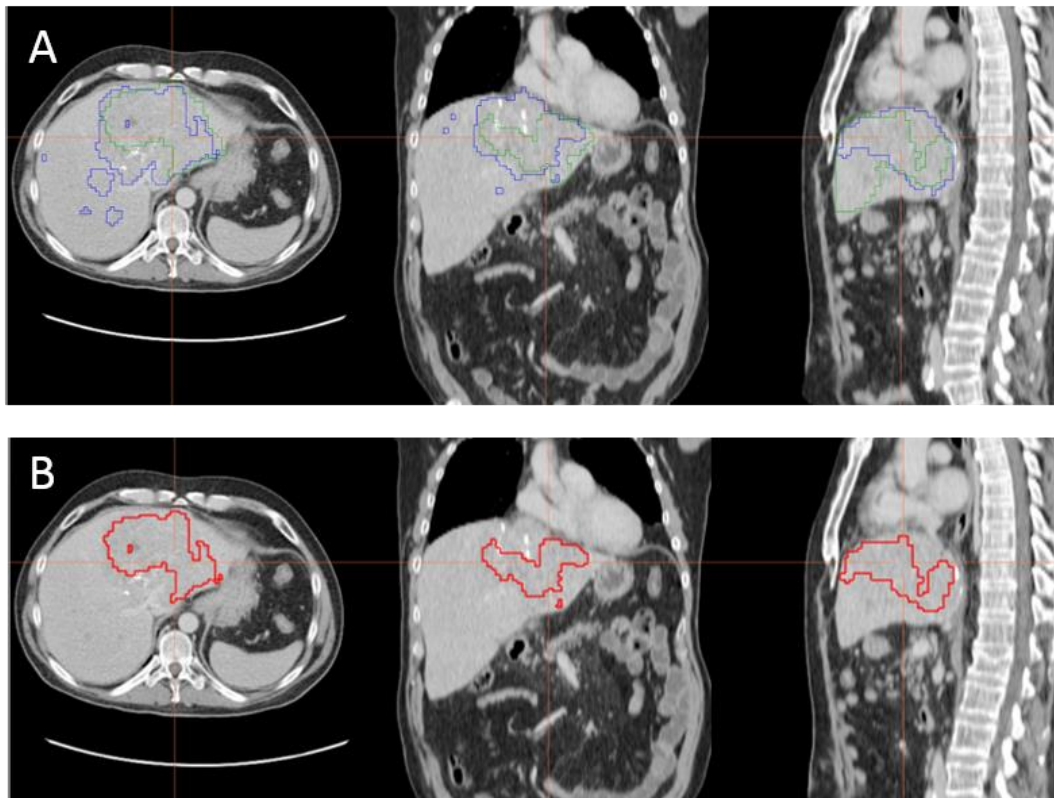
Figure 33 A: FEC-volume labeled in blue and MAA-volume marked with green color in the transverse, coronal and sagittal view (left to right). The combined volume of FEC- and MAA-volume marked with red color in transverse, coronal and sagittal view.

4　　Results and Discussion

First the results from the volumetric analysis are presented and discussed. In the subsequent chapter, the survival data from the patients are calculated and investigated and compared with the size of the intersection volume.

4.1　　Volumetric Analysis

The results of the volumetric analysis for each of the 24 patients before the SIRT was applied are listed in *Table 2*. The average total liver volume of all patients is 2028 ± 124 milliliter, similar to a healthy liver [4, 9]. The largest liver was determined to 3422 milliliter from a 56 old man and the smallest liver to 804 milliliter from a young woman. *Figure 35* displays the distribution of the total-liver volumes from all patients.

In order to define the threshold above which the FEC- and MAA-volumes were determined, reference values had to be set. In the case of the FEC-PET/CT scan the voxel, which was set into a supposedly healthy liver region yielded SUV-values. The threshold value was specified as 125% of the SUV_{peak} value. In *Table 3* the threshold values are listed for each patient. The average threshold was $10,81 \pm 0,37$. The MAA-SPECT-image is composed of gray scale units. Here, the threshold was specified as 200% of the reference voxel which was placed into a supposedly healthy liver region. The results are given in *Table 3*. The mean value of the MAA-threshold is $124,75 \pm 19,51$.

The blood-perfusion volume with the abbreviation MAA is found in the 4th column in *Table 2*. It consists of all liver regions with higher vascularization than the adjacent liver tissue. It does not necessarily indicate the real HCC-volume, since other liver regions without a tumorous tissue can have a higher vascularization too. In contrast, HCC's without any arterial access do not show any activity in the MAA-scan, and are, therefore, invisible and do not contribute to the tumor volume. The majority of the determined MAA-volumes range between 20 to 300 milliliter, except for one patient, which has a volume of 525 milliliter (see *Figure 34*).

The volume with elevated metabolic rate in comparison to the normal or healthy liver tissue is labeled with FEC in *Table 2*. FEC-volumes range from very small volumes

Table 2 The results from the volume determinations of all 24 patients. In the second column the volume of the total liver of each patient is listed. The abbreviation FEC describes the volumes with elevated metabolic rate in comparison to the normal or healthy adjacent liver tissue. The volumes with elevated vascularization are shown in the 4th column labeled MAA. The last column contains the intersection volumes from the metabolic and vascularization volume.

Name	Liver total [ml]	FEC [ml]	MAA [ml]	Combined [ml]
Patient #1	3421,6	742,8	524,9	358,1
Patient #2	1693,9	70,9	212,5	31,0
Patient #3	1603,9	21,6	31,8	2,3
Patient #4	2913,5	647,1	139,2	114,5
Patient #5	1124,8	137,2	261,2	31,5
Patient #6	1384,2	17,0	68,3	0,4
Patient #7	2262,1	150,0	51,3	30,0
Patient #8	2625,9	334,9	103,4	31,5
Patient #9	2360,8	289,1	35,7	1,7
Patient #10	1515,5	148,4	54,5	23,3
Patient #11	1769,2	60,5	35,1	1,5
Patient #12	2000,4	151,2	292,9	87,3
Patient #13	2205,7	68,2	159,2	14,1
Patient #14	2358,5	16,0	20,3	0,4
Patient #15	1272,0	72,5	192,2	53,4
Patient #16	2684,4	132,1	63,8	2,2
Patient #17	1893,1	82,6	41,6	5,1
Patient #18	804,2	2,7	19,6	0,1
Patient #19	2350,1	98,9	91,2	6,9
Patient #20	1949,0	220,6	60,8	44,7
Patient #21	1711,9	143,6	110,3	30,8
Patient #22	2340,1	37,3	242,8	6,1
Patient #23	1811,5	42,9	41,4	1,6
Patient #24	2606,7	172,3	292,9	15,1
Average	2027,6	160,8	131,1	37,2

of only 2,68 milliliter to larger volumes with approximately 742,8 milliliter. *Figure 36* reveals that only two patients have very large HCC volumes, while the majority of the volumes is in the order of 300 millimeter.

Overall, the average FEC-volume is about 161 ± 38 milliliter. As mentioned earlier the FEC-volume is a good indicator for the real position and size of the tumor. In *Table 4* the percentage of HCC to the total liver volume is summarized. The HCC content in

Table 3 Threshold values for the determination of the FEC- and MAA-Volumes.

Name	Threshold values	
	FEC [SUV]	MAA [gray scale]
Patient #1	10,0	213,2
Patient #2	15,3	165,6
Patient #3	12,1	287,0
Patient #4	12,3	76,0
Patient #5	15,9	174,0
Patient #6	17,1	238,0
Patient #7	12,4	159,4
Patient #8	14,3	270,0
Patient #9	10,5	190,4
Patient #10	17,3	159,0
Patient #11	13,6	222,0
Patient #12	12,7	63,4
Patient #13	13,8	205,8
Patient #14	10,8	281,0
Patient #15	16,5	316,0
Patient #16	16,0	196,0
Patient #17	13,4	160,0
Patient #18	13,6	433,6
Patient #19	10,1	298,0
Patient #20	15,2	218,0
Patient #21	12,1	1046,0
Patient #22	15,9	91,8
Patient #23	12,8	371,8
Patient #24	10,7	152,0
Average	13,5	249,5

relation to the total liver volume on average is about 7%. Note that some patients had already therapies and surgical interventions, which altered the tumor size.

The average MAA-volume is around 131 ± 25 milliliter. The percentages of elevated vascularization volumes to the corresponding total liver volumes are listed in *Table 4*. For all 24 patients that calculates to an average of $6,6\%$, slightly less than the FEC-volume part, described above.

Finally, the intersection volume of the elevated metabolic volume and the elevated vascularization volume is shown in the last column in *Table 2*. From *Figure 37* it can be seen, that only a few patients have large intersection volumes. Most of them have
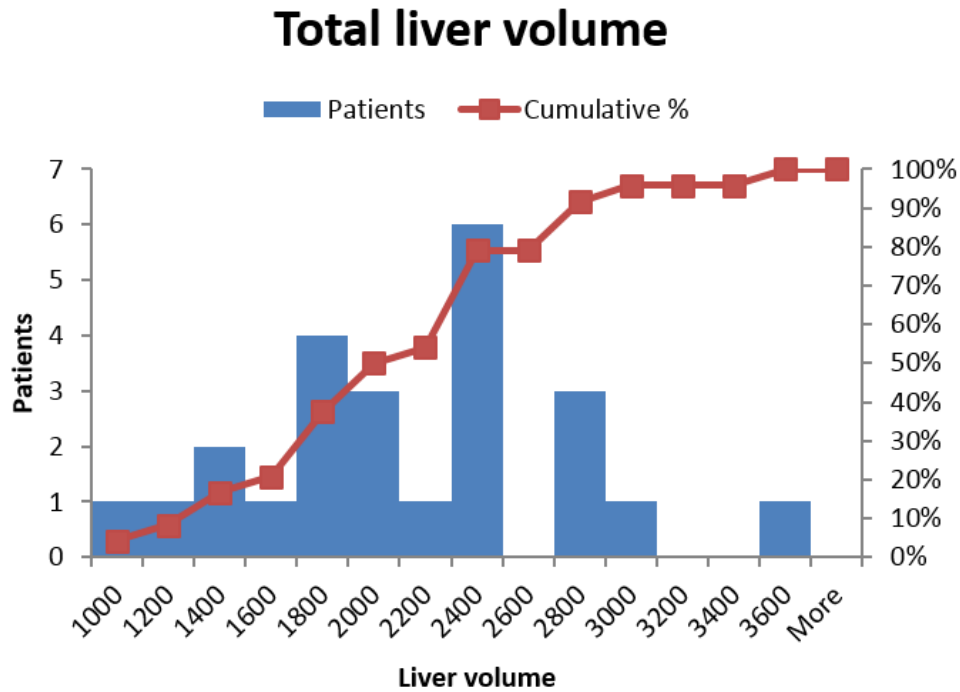
Total liver volume

Figure 35 Histogram of the total liver volumes from all 24 Patients.

Blood perfusion volume
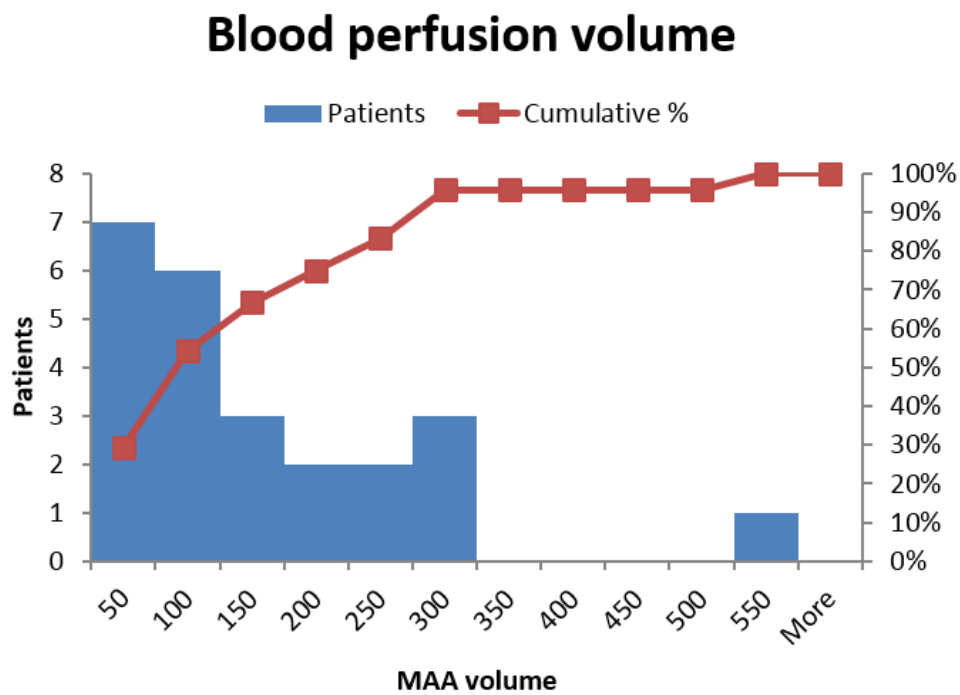
Figure 34 Histogram of the vascularization volumes from all 24 Patients.

a combined volume of a few centiliters. The average intersection volume of all patients is 37 ± 15 milliliter. The combined volume in relation to the total liver volume is on average only $1{,}6\%$. The single percentage values are calculated in *Table 4*.

Metabolic tumor volume
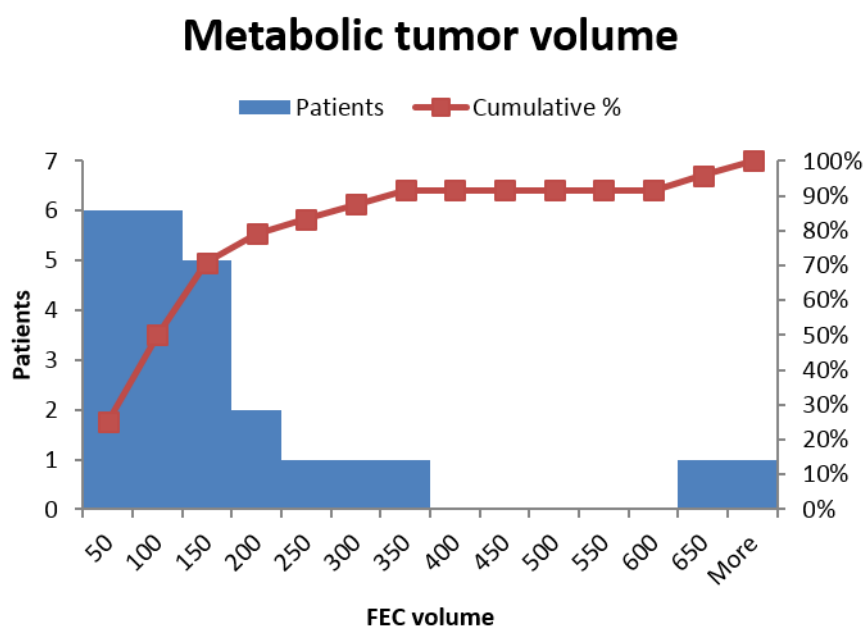
Figure 36 Histogram of the metabolic tumor volumes from all 24 Patients.

Intersection volume
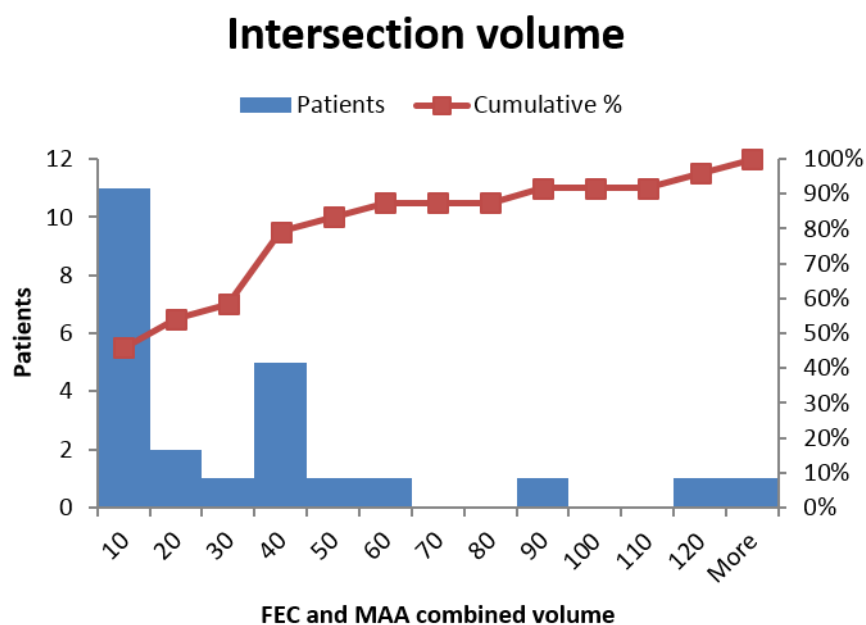
Figure 37 Histogram of the intersection volumes from all 24 Patients.

Table 4 Percentage of the volume in relationship to each other. Values in column two, three and four are in relation to the total liver volume, respectively. Column five describes the percentage of FEC-volumes, which have also a higher vascularization compared to the adjacent normal liver tissue are listed. Liver tissue. In the last column the percentages of MAA-volumes which have also a higher metabolic rate compared to the surrounding

Name	FEC - total	MAA - total	FEC&MAA - total	FEC&MAA - FEC	FEC&MAA - MAA
Patient #1	21,7%	15,3%	10,5%	48,2%	68,2%
Patient #2	4,2%	12,5%	1,8%	43,7%	14,6%
Patient #3	1,3%	2,0%	0,1%	10,7%	7,3%
Patient #4	22,2%	4,8%	3,9%	17,7%	82,2%
Patient #5	12,2%	23,2%	2,8%	22,9%	12,0%
Patient #6	1,2%	4,9%	0,0%	2,4%	0,6%
Patient #7	6,6%	2,3%	1,3%	20,0%	58,5%
Patient #8	12,8%	3,9%	1,2%	9,4%	30,5%
Patient #9	12,2%	1,5%	0,1%	0,6%	4,7%
Patient #10	9,8%	3,6%	1,5%	15,7%	42,7%
Patient #11	3,4%	2,0%	0,1%	2,5%	4,3%
Patient #12	7,6%	14,6%	4,4%	57,8%	29,8%
Patient #13	3,1%	7,2%	0,6%	20,7%	8,9%
Patient #14	0,7%	0,9%	0,0%	2,5%	2,0%
Patient #15	5,7%	15,1%	4,2%	73,7%	27,8%
Patient #16	4,9%	2,4%	0,1%	1,7%	3,5%
Patient #17	4,4%	2,2%	0,3%	6,2%	12,3%
Patient #18	0,3%	2,4%	0,0%	3,4%	0,5%
Patient #19	4,2%	3,9%	0,3%	6,9%	7,5%
Patient #20	11,3%	3,1%	2,3%	20,3%	73,6%
Patient #21	8,4%	6,4%	1,8%	21,5%	27,9%
Patient #22	1,6%	10,4%	0,3%	16,3%	2,5%
Patient #23	2,4%	2,3%	0,1%	3,8%	3,9%
Patient #24	6,6%	11,2%	0,6%	8,7%	5,1%
Average	7,0%	6,6%	1,6%	18,2%	22,1%

More important is the relationship between the combined volume and the metabolic- or vascularized volume. The percentage of metabolic volumes which are also well vascularized are given in the penultimate column of *Table 4*. The average value of all 24 patients is 18,22%. The amount of MAA-volumes which have a high metabolic rate are found in the last column of *Table 4*. Here, the average of all patients calculates to 22,12%. The results suggest that approximately 1/5 of the FEC-volume/MAA-volume is also well vascularized/well metabolized.

4.2 Survival data

The SIRT-Therapy was not recommended for six patients due to relevant liver-lung shunts. For the other eighteen patients the therapy was applied shortly after the FEC-PET/CT scan and the MAA scan. Usually, the time between scans and therapy were less than 3 weeks. Therefore, it can be assumed that the MAA-volumes and FEC-volumes did not change noticeable in this short period of time.

Twelve Patients received a second SIRT-Therapy after roughly a month. After two-to-three months, some of the patients were investigated again with a FEC-PET/CT scan, but too few for feasible investigations. Instead, the AFP-values and the number of survived days after the SIRT-Therapy are used for further evaluations and are given in *Table 5*. On average, the 18 patients lived 482 ± 80 days after the SIRT, which are approximately 16 months.

Comparing the results from *Table 2* with those from *Table 5* it can be seen, that some data are not conclusive. For instance, *Patient #4* and *Patient #9* have relative large FEC-volumes and an increased AFP after SIRT but rather long survival times with 1071 and 940 days, respectively. On the other hand, *Patient #1* with a large intersection of FEC- and MAA-volume survived only 126 days. *Figure 38* suggests that patients with smaller intersection of FEC- and MAA-volume survived longer than those with larger ones, by neglecting those individual cases mentioned above.

This can be understood with the following consideration. Small tumors in their early stages are usually poorly blood perfused since they have no yet established an arterial access. The smaller the tumor, the better the prognosis for the patient, although the SIRT-Therapy would benefit from a large intersection volume. In fact, *Figure 39* demonstrates that patients with smaller FEC-volumes have a slightly higher median survival. A cohort study of 502 HCC patients demonstrated that patients with a smaller vascularized tumor volume profit from SIRT [62]. This is in contradiction with the assumption that patients with large vascularized tumor volumes profit from SIRT.

Clearly, the tumor size is not solely responsible for the survival. In fact, the interaction of tumor size with liver function, underlying diseases and overall health status determines the median survival. The assumption that patients with a large intersection volume benefit from SIRT-Therapy is in this thesis not confirmed.

Table 5 AFP-values before and after SIRT-Therapy from 18 patients with the change and the progress. Furthermore, the age and the survived days are listed for every patient, respectively

Name	AFP pre	AFP post	AFP Δ %	Progress	Age	Days after Treatment
Patient #1	11,2	69,9	524,1%	Negative	56	126
Patient #2	40	121	202,5%	Negative	67	139
Patient #3	1120	790	-29,5%	Positive	79	274
Patient #4	15	23	53,3%	Negative	77	1071
Patient #6	20	8,8	-56,0%	Positive	59	98
Patient #7	85000	9000	-89,4%	Positive	67	236
Patient #9	64	900	1306,3%	Negative	77	940
Patient #10	11140	3540	-68,2%	Positive	64	370
Patient #12	61	106	73,8%	Negative	66	175
Patient #13	3,2	5,6	75,0%	Negative	70	412
Patient #14	15	13	-13,3%	Positive	67	934
Patient #15	1300	200	-84,6%	Positive	61	388
Patient #16	1700	1300	-23,5%	Positive	66	526
Patient #17	12	29	141,7%	Negative	74	1057
Patient #19	130000	462000	255,4%	Negative	60	196
Patient #20	43,4	2583	5851,6%	Negative	82	303
Patient #23	8	5	-37,5%	Positive	65	844
Patient #24	82,8	72,5	-12,4%	Positive	60	578
Average	12813,1	26709,3	448,3%		67,6	481,5
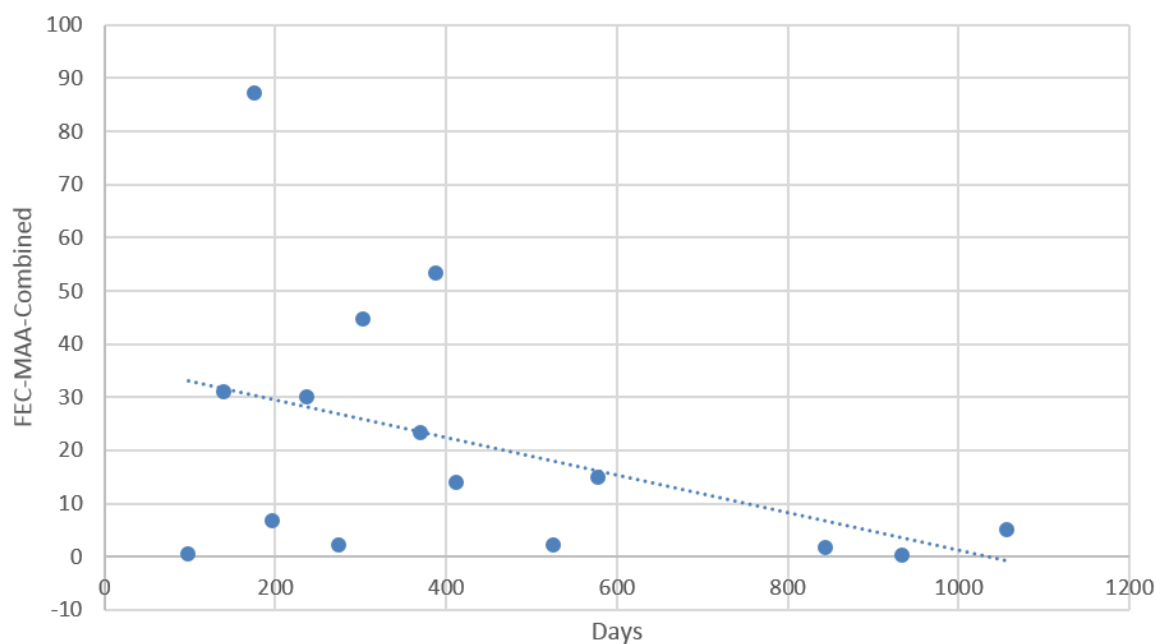
Figure 38 Graph of combined volume consisting of metabolic tumor volume and vascularization volume versus days survived after SIRT. The trend line suggests that patients with smaller combined volumes lived longer.
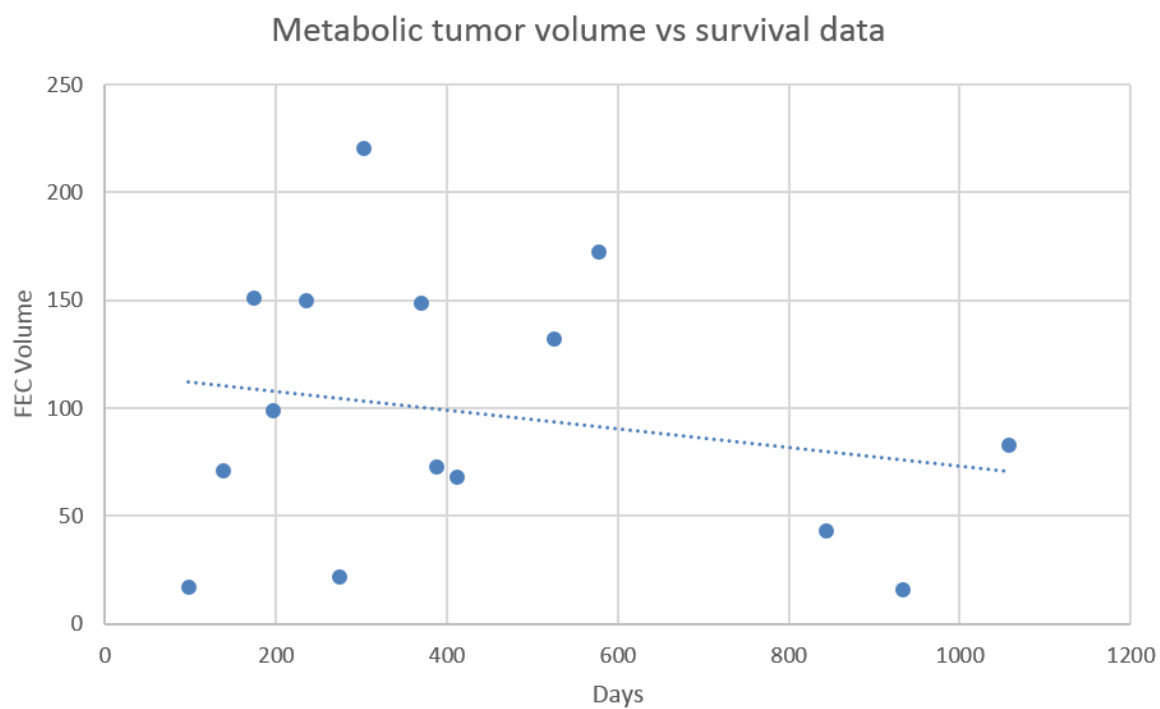
Figure 39 Graph of metabolic tumor versus days survived after SIRT. The trend line suggests that patients with smaller metabolic tumor volumes lived longer.

4.3　ROC-Analysis

The Receiver Operating Characteristics (ROC) curves are used to illustrate the impact of the determined variables compared with the outcome, i.e. the median survival of the 24 HCC patients. *Figure 40* shows the ROC analysis of the combined volume (FEC+MAA) and the fraction of metabolic tumor volume which is highly vascularized in comparison with the mean survival in HCC patients. The black curve in *Figure 40* represents the intersection volume of the metabolic and vascularization volume. It has an Area under the Curve (AUC) of 0.63 and a p-value of 0.298 and is therefore not significant. On the other hand, the red curve representing the fraction of the metabolic tumor volume which is also well vascularized is significant with an AUC of 0.75 and a p-value of 0.048. Patients with a metabolic tumor volume with an increased vascularization have a poorer prognosis compared to patients with a poorly blood perfused metabolic tumor volume.

ROC analyses with the AFP-values before and after the therapy from each patients resulted in this thesis in curves without any significance. Although, it has been proven that AFP is an important independent prognostic factor for HCC patients [63, 64].

During the volumetric analysis also other variables were collected, such as the mean SUV value and the background-corrected peak and mean SUV value of the liver (see *Table 6*). These values on their own are not significant in the ROC-analysis, but, together with the total liver volume, the intersection volume and the metabolic tumor volume with high vascularization, they contribute as variables in a multiple regression analysis. In *Equation 14* it can be seen that the multiple regression is composed of those six variables with prefactors. The result is significant with an AUC of 0.87 and a p value of 0.004. In this calculation only one parameter was significant at the beginning, i.e. the metabolic tumor volume with a high vascularization. The other parameters were not significant, however, not one single parameter but rather the combination of all these parameters results in a curve which is highly significant.

$$
\begin{aligned}
\text{Multi regression analysis} \hspace{4cm} & (14)\\
= -0{,}815 \hspace{5cm} & \\
- (0{,}0494 * SUV \text{ liver mean}) \hspace{2.5cm} & \\
- (0{,}823 * SUV \text{ TBR max}) \hspace{2.8cm} & \\
+ (0{,}785 * SUV \text{ TBR peak}) \hspace{2.7cm} & \\
+ (0{,}00134 * \text{Liver total vol}) \hspace{2.6cm} & \\
+ (0{,}00405 * FEC + \text{MAA vol}) \hspace{2.4cm} & \\
- (13{,}549 * \%\text{MAA pos FEC Vol}) \hspace{2cm} &
\end{aligned}
$$
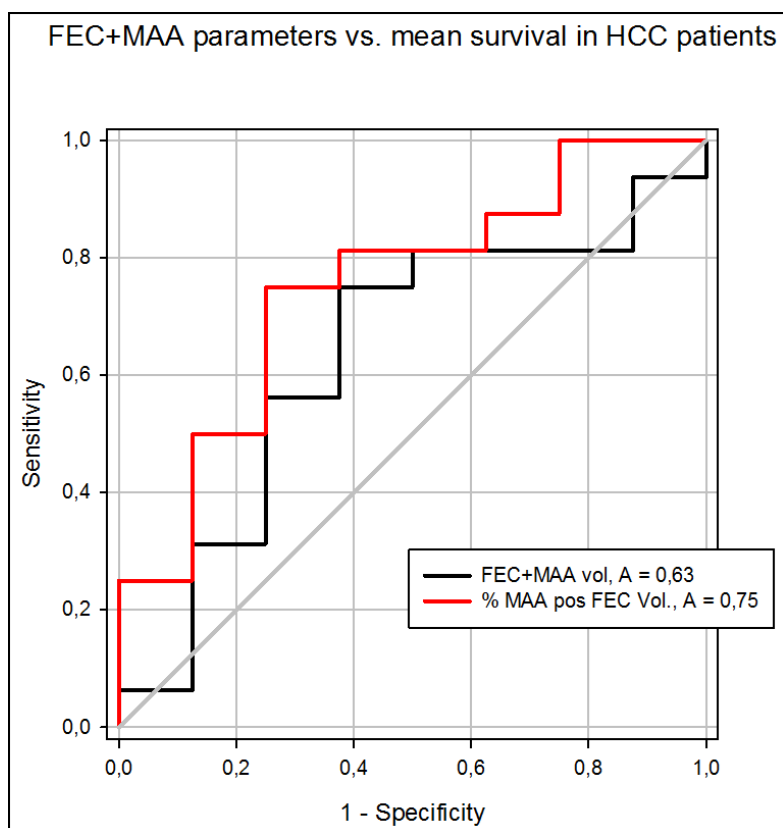
Figure 40 ROC-Analysis of the combined volume (FEC+MAA) versus the mean survival in HHC patients in black and the metabolic tumor volume with high vascularization in red.
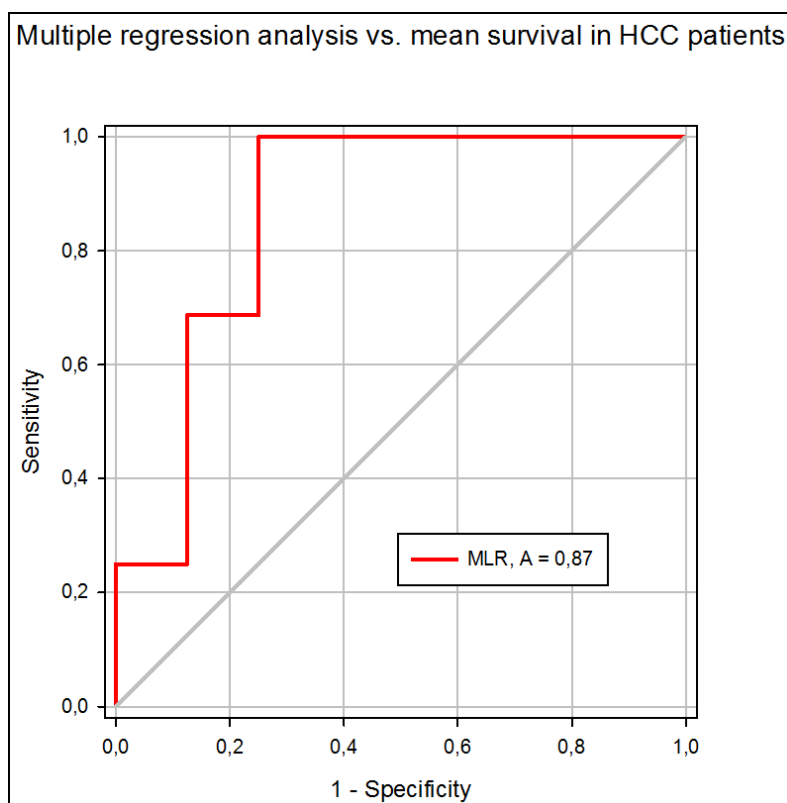
Figure 41 Multiple logistic regression analysis versus the mean survival in HHC patients.

Table 6 Variables for the multiple logistic regression analysis.

Pat.Nr.	Days PET-Death	FEC+MAA vol [ml]	% MAA pos FEC Vol.	SUV liver mean	SUV TBR max	SUV TBR peak	Liver total vol [ml]
Patient #1	170	358,1	48,2%	17,0	6,3	7,2	3421,6
Patient #2	176	31,0	43,7%	16,4	4,8	5,0	1693,9
Patient #3	316	2,3	10,7%	13,8	3,8	4,2	1603,9
Patient #4	1122	114,5	17,7%	17,7	7,5	8,8	2913,5
Patient #5	1029	31,5	22,9%	16,9	4,8	4,8	1124,8
Patient #6	204	0,4	2,4%	17,7	2,9	3,2	1384,2
Patient #7	446	30,0	20,0%	14,3	3,2	3,2	2262,1
Patient #8	42	31,5	9,4%	16,2	5,3	6,0	2625,9
Patient #9	947	1,7	0,6%	11,5	3,4	3,2	2360,8
Patient #10	399	23,3	15,7%	18,7	4,6	4,6	1515,5
Patient #11	241	1,5	2,5%	14,5	3,8	3,6	1769,2
Patient #12	274	87,3	57,8%	17,0	5,6	5,6	2000,4
Patient #13	450	14,1	20,7%	17,7	5,4	5,5	2205,7
Patient #14	992	0,4	2,5%	11,4	2,7	3,0	2358,5
Patient #15	395	53,4	73,7%	20,3	4,3	3,9	1272,0
Patient #16	532	2,2	1,7%	19,5	7,4	7,2	2684,4
Patient #17	1099	5,1	6,2%	14,6	3,7	3,6	1893,1
Patient #18	173	0,1	3,4%	14,1	3,1	3,5	804,2
Patient #19	198	6,9	6,9%	11,3	4,3	4,3	2350,1
Patient #20	355	44,7	20,3%	23,9	15,5	15,1	1949,0
Patient #21	23	30,8	21,5%	13,4	3,5	5,2	1711,9
Patient #22	333	6,1	16,3%	17,1	4,0	4,1	2340,1
Patient #23	860	1,6	3,8%	14,1	4,7	4,9	1811,5
Patient #24	585	15,1	8,7%	11,5	4,4	4,9	2606,7
Average	473,4	37,2	18,2%	15,9	4,9	5,2	2027,6

The last step was the calculation of the Kaplan-Meier curve, which represents the survival probability of the patients over time (see *Figure 42*). It was calculated by taking the cut-off value from the multiple regression curve, which is shown in *Figure 41* at sensitivity one and approximately 0.75 specificity. 18 patients in whom the volumetric and the multiple regression analysis predicted a short median survival have in fact shorter life expectancy, represented with the red curve in *Figure 42*. On the other hand, the green curve expresses six patients in whom the volumetric and the multiple logistic regression analysis predicted a longer median survival and indeed a higher median survival was found. The green curve in *Figure 42* has a significance of 0.017.

Considering the small collective of patients the multiple regression analysis shows promising results.
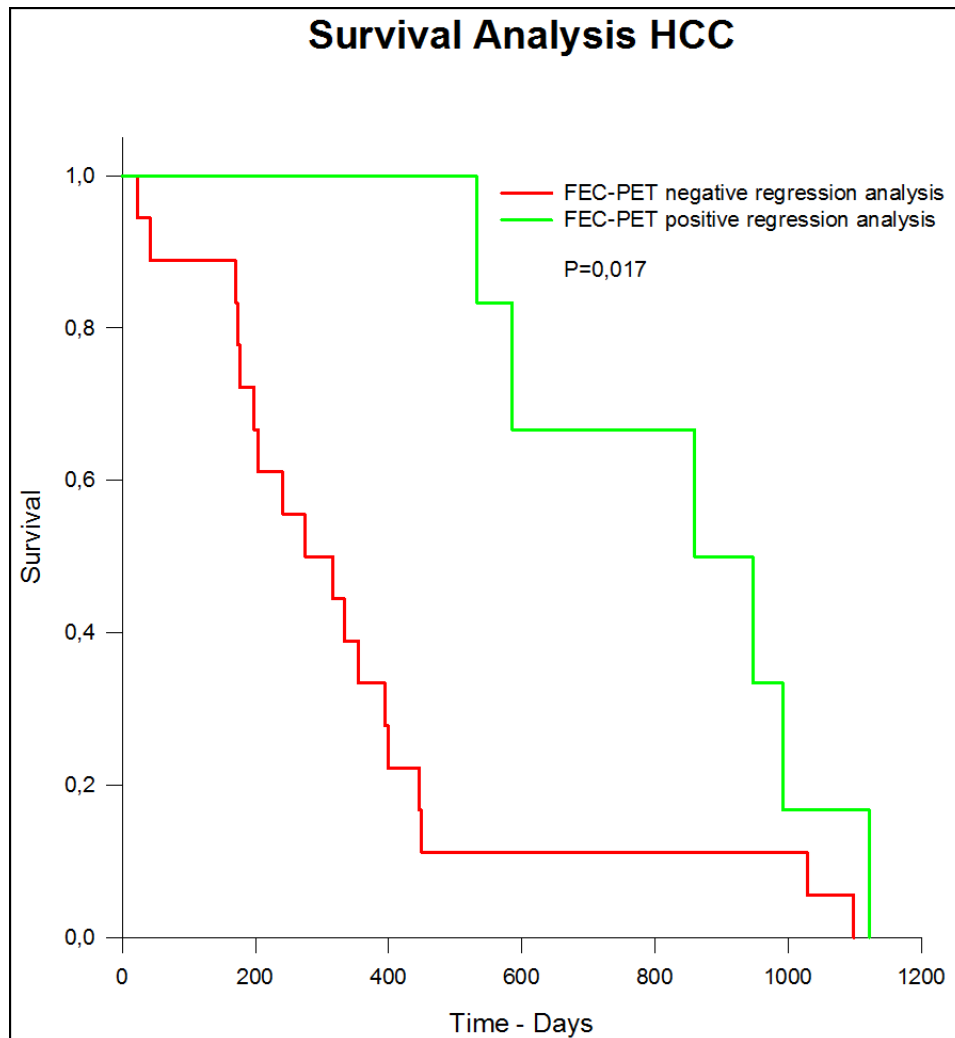
Figure 42 Kaplan-Meier curve showing the survival probability. Patients in whom a short median survival was predicted had in fact a lower median survival (red curve), while patients in whom a longer survival was predicted lived on average longer (green curve).

5   Conclusion

The knowledge of tumor vascularization is an important factor regarding prognosis and therapy selection for HCC patients. HCC is characterized by arterial hypervascularity as a consequence of its high oxygen and nutrient demand. This fact is used by the palliative treatment SIRT, where small radioactive spheres are injected via the hepatic artery to the malignancies yielding to irradiation of HCC and blocking of the tumor capillaries.

The aim of this study was to evaluate prognostic parameters from a volumetric analysis of 24 HCC patients and compare the results with the survival data of the latter.

The average total liver volume of all HCC patients was determined to 2028 ± 124 milliliter. The average vascularization volume and the metabolic tumor volume were calculated to 131 ± 25 milliliter and 161 ± 38 milliliter, respectively. The intersection volume of those volumes is approximately $37,2 \pm 15,1$ milliliter. Further, the metabolic tumor volume which is also highly vascularized in relation to the whole tumor volume was calculated to $18,22\%$.

The results from the volumetric analysis were compared to the survival data of each patient. From the intersection volume it can be concluded, that patients with smaller combined volumes are more likely to survive longer than patients with larger combined volumes. This rather obvious result is in contradiction with the assumption that SIRT profits from larger tumors but was also confirmed in the cohort study from Ilhan et al [62]. This cohort study of 502 patients demonstrates that patients with small vascularization volumes profit from SIRT and have on average a higher median survival compared to patients with larger vascularized HCCs.

A ROC-analysis of the intersection volume in comparison with the survival data was not significant with an AUC of only 0.63. It confirms that the size of the metabolic tumor volume is not solely responsible for survival prediction. The AFP-values measured before and after the SIRT were also not significant in this study, although, AFP has been proven to be an important independent prognostic factor for HCC patients [63, 64].

The fraction of metabolic tumor volume which is well vascularized was significant in this study with an AUC of 0.75 and a p-value of 0.045, i.e. patients with a large vascularized metabolic-active tumor volume present poor prognosis compared to patients with little vascularized metabolic-active tumor volume.

Other parameters such as the mean SUV value and the background-corrected peak and mean SUV value of the liver showed no significance mainly due to the low number of HCC patients investigated in this study, but they were used as variables in a multiple

logistic regression analysis. This analysis was highly significant, when combining all parameters together. Therefore, not a single parameter is the key to a reliable prediction, but rather the combination of several independent parameters. Further, multi-parametric imaging of metabolic parameters are more reliable than single morphological parameters, such as the tumor size.

This thesis shows that with the given diagnostic methods and current software, multiple metabolic parameters can be combined and compared in order to describe and understand various mechanisms within body. These information are of major importance regarding prognosis of life expectancy and suitability for therapies, such as SIRT.

Further studies with a larger collective of patients are necessary to quantify the results gained from this thesis. However, this thesis shows the potential of the volumetric analysis in HCC patients.

6   Bibliography

1.   European Association for the Study of the Liver and European Organisation for Research Treatment of Cancer, *EASL-EORTC clinical practice guidelines: management of hepatocellular carcinoma.* J Hepatol, 2012. 56(4): p. 908-43.

2.   World Health Organization, *Global battle against cancer won't be won with treatment alone Effective prevention measures urgently needed to prevent cancer crisis.* Lyon, London: International Agency for Research on Cancer, 2014.

3.   Parkin, D.M., et al., *Global cancer statistics, 2002.* CA Cancer J Clin, 2005. 55(2): p. 74-108.

4.   Lippert, H., *Lehrbuch Anatomie.* 2003: Elsevier Health Sciences Germany.

5.   Sangro, B., *Chemoembolization and radioembolization.* Best Pract Res Clin Gastroenterol, 2014. 28(5): p. 909-19.

6.   Sangro, B., M. Inarrairaegui, and J.I. Bilbao, *Radioembolization for hepatocellular carcinoma.* J Hepatol, 2012. 56(2): p. 464-73.

7.   World Health Organization. *Hepatitis B.* 2015 14 April]; Fact sheet N°204 [Available from: http://www.who.int/mediacentre/factsheets/fs204/en/.

8.   World Health Organization. *Hepatitis C.* 2014 [cited 2015 16 April]; Fact sheet N°164:[Available from: http://www.who.int/mediacentre/factsheets/fs164/en/.

9.   *Essentials of Rubin's Pathology.* 2008: Lippincott Williams & Wilkins.

10.   Raza, A. and G.K. Sood, *Hepatocellular carcinoma review: current treatment, and evidence-based medicine.* World J Gastroenterol, 2014. 20(15): p. 4115-27.

11.   Zhu, A.X., et al., *HCC and angiogenesis: possible targets and future directions.* Nat Rev Clin Oncol, 2011. 8(5): p. 292-301.

12.   Llovet, J.M. and J. Bruix, *Novel advancements in the management of hepatocellular carcinoma in 2008.* J Hepatol, 2008. 48 Suppl 1: p. S20-37.

13.   El-Serag, H.B. and A.C. Mason, *Rising incidence of hepatocellular carcinoma in the United States.* N Engl J Med, 1999. 340(10): p. 745-50.

14.   Bosetti, C., et al., *Trends in mortality from hepatocellular carcinoma in Europe, 1980-2004.* Hepatology, 2008. 48(1): p. 137-45.

15.   El-Serag, H.B., *Epidemiology of viral hepatitis and hepatocellular carcinoma.* Gastroenterology, 2012. 142(6): p. 1264-1273 e1.

16. Forner, A., J.M. Llovet, and J. Bruix, *Hepatocellular carcinoma.* Lancet, 2012. 379(9822): p. 1245-55.

17. Sangiovanni, A., et al., *The natural history of compensated cirrhosis due to hepatitis C virus: A 17-year cohort study of 214 patients.* Hepatology, 2006. 43(6): p. 1303-10.

18. El-Serag, H.B., P.A. Richardson, and J.E. Everhart, *The role of diabetes in hepatocellular carcinoma: a case-control study among United States Veterans.* Am J Gastroenterol, 2001. 96(8): p. 2462-7.

19. Marrero, J.A., et al., *Alcohol, tobacco and obesity are synergistic risk factors for hepatocellular carcinoma.* J Hepatol, 2005. 42(2): p. 218-24.

20. Marcellin, P., et al., *Mortality related to chronic hepatitis B and chronic hepatitis C in France: evidence for the role of HIV coinfection and alcohol consumption.* J Hepatol, 2008. 48(2): p. 200-7.

21. Coulon, S., et al., *Angiogenesis in chronic liver disease and its complications.* Liver Int, 2011. 31(2): p. 146-62.

22. Sun, X.T., et al., *Endothelial precursor cells promote angiogenesis in hepatocellular carcinoma.* World J Gastroenterol, 2012. 18(35): p. 4925-33.

23. Yamamoto, T., et al., *Sinusoidal capillarization and arterial blood supply continuously proceed with the advance of the stages of hepatocarcinogenesis in the rat.* Jpn J Cancer Res, 1996. 87(5): p. 442-50.

24. Bolondi, L., et al., *Characterization of small nodules in cirrhosis by assessment of vascularity: the problem of hypovascular hepatocellular carcinoma.* Hepatology, 2005. 42(1): p. 27-34.

25. Forner, A., et al., *Diagnosis of hepatic nodules 20 mm or smaller in cirrhosis: Prospective validation of the noninvasive diagnostic criteria for hepatocellular carcinoma.* Hepatology, 2008. 47(1): p. 97-104.

26. Borzio, M., et al., *Impact of large regenerative, low grade and high grade dysplastic nodules in hepatocellular carcinoma development.* J Hepatol, 2003. 39(2): p. 208-14.

27. Gomaa, A.I. and I. Waked, *Recent advances in multidisciplinary management of hepatocellular carcinoma.* World J Hepatol, 2015. 7(4): p. 673-87.

28. Roskams, T. and M. Kojiro, *Pathology of early hepatocellular carcinoma: conventional and molecular diagnosis.* Semin Liver Dis, 2010. 30(1): p. 17-25.

29. Stigliano, R., et al., *Seeding following percutaneous diagnostic and therapeutic approaches for hepatocellular carcinoma. What is the risk and the outcome? Seeding risk for percutaneous approach of HCC.* Cancer Treat Rev, 2007. 33(5): p. 437-47.

30. Llovet, J.M., et al., *Natural history of untreated nonsurgical hepatocellular carcinoma: rationale for the design and evaluation of therapeutic trials.* Hepatology, 1999. 29(1): p. 62-7.

31. Roskams, T., *Anatomic pathology of hepatocellular carcinoma: impact on prognosis and response to therapy.* Clin Liver Dis, 2011. 15(2): p. 245-59, vii-x.

32. Bruix, J., M. Sherman, and D. American Association for the Study of Liver, *Management of hepatocellular carcinoma: an update.* Hepatology, 2011. 53(3): p. 1020-2.

33. Llovet, J.M., C. Bru, and J. Bruix, *Prognosis of hepatocellular carcinoma: the BCLC staging classification.* Semin Liver Dis, 1999. 19(3): p. 329-38.

34. Kudo, M., *Review of 4th Single Topic Conference on HCC. Hepatocellular carcinoma: International consensus and controversies.* Hepatol Res, 2007. 37 Suppl 2: p. S83-7.

35. Takayama, T., et al., *Early hepatocellular carcinoma as an entity with a high rate of surgical cure.* Hepatology, 1998. 28(5): p. 1241-6.

36. Livraghi, T., et al., *Sustained complete response and complications rates after radiofrequency ablation of very early hepatocellular carcinoma in cirrhosis: Is resection still the treatment of choice?* Hepatology, 2008. 47(1): p. 82-9.

37. Llovet, J.M. and J. Bruix, *Systematic review of randomized trials for unresectable hepatocellular carcinoma: Chemoembolization improves survival.* Hepatology, 2003. 37(2): p. 429-42.

38. Cabibbo, G., et al., *A meta-analysis of survival rates of untreated patients in randomized clinical trials of hepatocellular carcinoma.* Hepatology, 2010. 51(4): p. 1274-83.

39. Llovet, J.M., et al., *Sorafenib in advanced hepatocellular carcinoma.* N Engl J Med, 2008. 359(4): p. 378-90.

40. Beard, R.E., et al., *A comparison of surgical outcomes for noncirrhotic and cirrhotic hepatocellular carcinoma patients in a Western institution.* Surgery, 2013. 154(3): p. 545-55.

41. Bruix, J., et al., *Surgical resection of hepatocellular carcinoma in cirrhotic patients: prognostic value of preoperative portal pressure.* Gastroenterology, 1996. 111(4): p. 1018-22.

42. Mazzaferro, V., et al., *Liver transplantation for the treatment of small hepatocellular carcinomas in patients with cirrhosis.* N Engl J Med, 1996. 334(11): p. 693-9.

43. Lencioni, R., et al., *Treatment of small hepatocellular carcinoma with percutaneous ethanol injection. Analysis of prognostic factors in 105 Western patients.* Cancer, 1995. 76(10): p. 1737-46.

44. Chang, Y.S., et al., *Sorafenib (BAY 43-9006) inhibits tumor growth and vascularization and induces tumor apoptosis and hypoxia in RCC xenograft models.* Cancer Chemother Pharmacol, 2007. 59(5): p. 561-74.

45. Salem, R., et al., *Radioembolization for hepatocellular carcinoma using Yttrium-90 microspheres: a comprehensive report of long-term outcomes.* Gastroenterology, 2010. 138(1): p. 52-64.

46. Hilgard, P., et al., *Radioembolization with yttrium-90 glass microspheres in hepatocellular carcinoma: European experience on safety and long-term survival.* Hepatology, 2010. 52(5): p. 1741-9.

47. Salem, R., et al., *Radioembolization results in longer time-to-progression and reduced toxicity compared with chemoembolization in patients with hepatocellular carcinoma.* Gastroenterology, 2011. 140(2): p. 497-507 e2.

48. Cherry, S.R., J.A. Sorenson, and M.E. Phelps, *chapter 13 - The Gamma Camera: Basic Principles*, in *Physics in Nuclear Medicine (Fourth Edition)*, S.R.C.A.S.E. Phelps, Editor. 2012, W.B. Saunders: Philadelphia. p. 195-208.

49. Cherry, S.R., J.A. Sorenson, and M.E. Phelps, *chapter 17 - Single Photon Emission Computed Tomography*, in *Physics in Nuclear Medicine (Fourth Edition)*, S.R.C.A.S.E. Phelps, Editor. 2012, W.B. Saunders: Philadelphia. p. 279-306.

50. Committee, E.P., et al., *Routine quality control recommendations for nuclear medicine instrumentation.* Eur J Nucl Med Mol Imaging, 2010. 37(3): p. 662-71.

51. Zanzonico, P., *Routine Quality Control of Clinical Nuclear Medicine Instrumentation: A Brief Review.* Journal of nuclear medicine : official publication, Society of Nuclear Medicine, 2008. 49(7): p. 1114-1131.

52. Graham, L.S., *Quality control for SPECT systems.* Radiographics, 1995. 15(6): p. 1471-81.

53. Turkington, T.G., *Introduction to PET Instrumentation.* Journal of Nuclear Medicine Technology, 2001. 29(1): p. 4-11.

54. Cherry, S.R., J.A. Sorenson, and M.E. Phelps, *chapter 18 - Positron Emission Tomography*, in *Physics in Nuclear Medicine (Fourth Edition)*, S.R.C.A.S.E. Phelps, Editor. 2012, W.B. Saunders: Philadelphia. p. 307-343.

55. Evans, R.D., *The atomic nucleus.* 1982, Malabar, Fla.: R.E. Krieger. xv, 972 p.

56. Fahey, F.H., *Data Acquisition in PET Imaging.* Journal of Nuclear Medicine Technology, 2002. 30(2): p. 39-49.

57. Townsend, D.W., et al., *A rotating PET scanner using BGO block detectors: design, performance and applications.* J Nucl Med, 1993. 34(8): p. 1367-76.

58. Beyer, T., et al., *A combined PET/CT scanner for clinical oncology.* J Nucl Med, 2000. 41(8): p. 1369-79.

59. Townsend, D.W., *Combined PET/CT: the historical perspective.* Seminars in ultrasound, CT, and MR, 2008. 29(4): p. 232-235.

60. Kinahan, P.E. and J.W. Fletcher, *PET/CT Standardized Uptake Values (SUVs) in Clinical Practice and Assessing Response to Therapy.* Seminars in ultrasound, CT, and MR, 2010. 31(6): p. 496-505.

61. Bieze, M., et al., *Diagnostic accuracy of (18) F-methylcholine positron emission tomography/computed tomography for intra- and extrahepatic hepatocellular carcinoma.* Hepatology, 2014. 59(3): p. 996-1006.

62. Ilhan, H., et al., *Systematic evaluation of tumoral 99mTc-MAA uptake using SPECT and SPECT/CT in 502 patients before 90Y radioembolization.* J Nucl Med, 2015. 56(3): p. 333-8.

63. Ma, W.J., H.Y. Wang, and L.S. Teng, *Correlation analysis of preoperative serum alpha-fetoprotein (AFP) level and prognosis of hepatocellular carcinoma (HCC) after hepatectomy.* World J Surg Oncol, 2013. 11: p. 212.

64. Xia, Y., et al., *A case-control study of correlation between preoperative serum AFP and recurrence of hepatocellular carcinoma after curative hepatectomy.* Hepatogastroenterology, 2012. 59(119): p. 2248-54.

7 Table of Figures

8   List of Tables